aerospace

Article

Numerical Investigation on Unsteady Shock Wave/Vortex/Turbulent Boundary Layer Interactions of a Hypersonic Vehicle during Its Shroud Separation

Pengcheng Cui, Hongyin Jia, Jiangtao Chen, Guiyu Zhou, Xiaojun Wu, Mingsheng Ma, Huan Li * and Jing Tang *

Computational Aerodynamics Institute, China Aerodynamics Research and Development Center,
Mianyang 621000, China
* Correspondence: lanzhongze2008@126.com (H.L.); pccui@foxmail.com (J.T.)

Abstract: Hypersonic vehicles are drawing more and more attention now and for the near future, especially in the low-altitudes near space, from 20 km to 45 km. The reliable separation of the protecting shroud from the hypersonic vehicle is a prerequisite and critical issue for the success of the entire flight mission. The unsteady multi-body separation characteristics and flow characteristics of hypersonic shroud separation at Mach 7.0 are investigated based on numerical simulation in this paper. The improved delayed detached eddy simulation (IDDES) method, dynamic hybrid overset mesh method, and HLLE++ numerical scheme are used to ensure numerical accuracy. Numerical results show that there are four types of vortexes and three types of shock waves inside the shrouds during the separation process, which generate complex shock wave/vortex/boundary layer interactions. Further, an unsteady process of the expansion-transfer-dissipation of an A-type vortex is found, which is the result of strong shock/vortex/boundary layer interactions. The adverse pressure gradient is the root cause driving the generation and transfer of the A-type vortex during the shroud separation. Furthermore, the transfer process of the A-type vortex only lasts for 5.52 ms but causes a large disturbance to the aerodynamic force of the shroud. The results of this paper could provide a reference for the design of near-space hypersonic vehicles.

Keywords: multi-body separation; hypersonic; numerical simulation; shock wave; vortex; boundary layer

check for updates

Citation: Cui, P.; Jia, H.; Chen, J.; Zhou, G.; Wu, X.; Ma, M.; Li, H.; Tang, J. Numerical Investigation on Unsteady Shock Wave/Vortex/Turbulent Boundary Layer Interactions of a Hypersonic Vehicle during Its Shroud Separation. *Aerospace* **2022**, *9*, 619. https://doi.org/10.3390/aerospace9100619

Academic Editor: Kung-Ming Chung

Received: 27 September 2022
Accepted: 17 October 2022
Published: 19 October 2022

1. Introduction

With the rapid development of aerospace technology, hypersonic vehicles are drawing more and more attention now and for the near future, especially in the low-altitudes near space of 20 km to 45 km [1–3]. For example, many countries have developed quite a few hypersonic vehicles; Table 1 only lists some typical hypersonic vehicles. The protecting shroud is an important part of the hypersonic vehicle. When the vehicle is flying at hypersonic speed in the dense atmosphere of near space, the shroud is utilized to protect the internal devices of the vehicle from being affected by harmful environments such as serious aerodynamic force, aerodynamic heat, and acoustic vibration. In addition, the shroud keeps the vehicle in a good aerodynamic configuration and reduces the drag of the vehicle. When the vehicle arrives at a certain area, the shroud must be dropped so that the vehicle can function normally and complete its work (Figure 1). The reliable separation of the protecting shroud from the hypersonic vehicle is a prerequisite and critical issue for the success of the entire flight mission.

Table 1. Typical hypersonic vehicles in the low-altitude near space.

Hypersonic Vehicles	**Velocity (Mach)**	**Altitude (km)**
HTV-2 (America)	5–7	20–40
ARRW (America)	6.5–8	20–35
Dagger (Russia)	6–10	20–35
Zircon (Russia)	5–9	unknown
DF-17 (China)	unknown	unknown
DF-XX (China)	unknown	unknown
HSTDV (India)	6	20–30

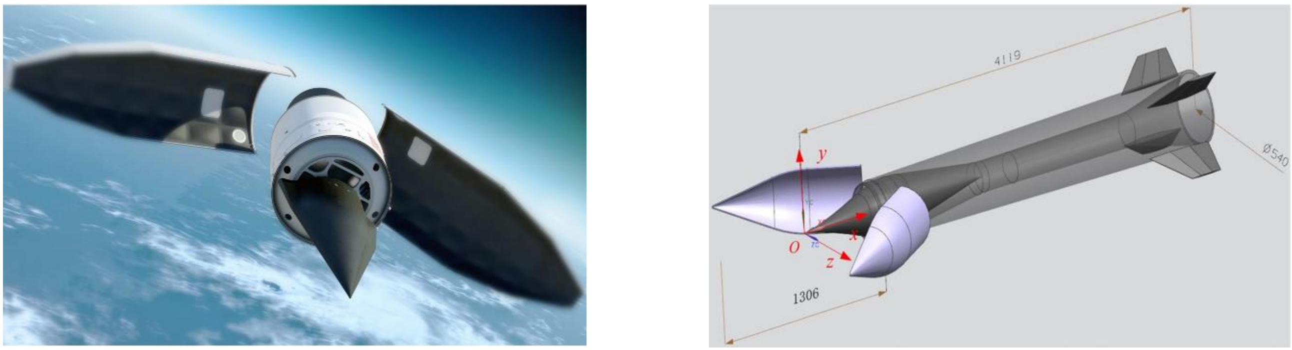

(**a**) (**b**)

Figure 1. Shroud separation of hypersonic vehicles: (**a**) shroud separation of hypersonic technology vehicle #2 (HTV-2) [4]; (**b**) shroud separation of hypersonic air-breathing vehicle (HAV) [5]. Figure adapted with permission from Wang et al. (2017). Copyright © 2017 American Institute of Aeronautics and Astronautics (AIAA).

Many researchers have studied shroud separation, but, as presented in Table 2, most of the research focuses on the rocket shroud separation in a thin atmosphere, or shroud separation at a Mach number lower than 5.0. Guthrie and Zaitsev studied the load characteristics during the shroud separation of a rocket in outer space [6,7] and Whalley introduced the development of the STARS II shroud separation system in outer space [8]. Tsutsumi investigated the flow characteristics of the shroud separation at Mach 0.8 based on hybrid LES/RANS simulations [9], Dagan and Arad analyzed the multi-bodies separation characteristics of the shroud releasing at Mach 2.5 based on unsteady numerical method and rigid body dynamics [10], Chamberlain studied the HEDI shroud separation based on the time-accurate finite element method [11], and Raj investigated the separation dynamics of fairings at test conditions based on an Euler solver [12].

A hypersonic vehicle operating in near space, which usually cruise at an altitude of 20 km to 45 km and under a Mach number of 6–8, is a new research field, though the multi-body separation has always been a focus and a difficulty [13]. However, current research on the multi-body separation of hypersonic vehicles mainly focuses on the stage separation of the booster and vehicle or the separation of the vehicle from the transport aircraft. So far, there are very limited studies that focus on the shroud separation from a hypersonic vehicle in the low-altitude near space. Holden investigated the multi-bodies separation characteristics of a hypersonic vehicle based on a "free flight" wind tunnel experiment [14]. Wang studied the shroud separation with a hypersonic air-breathing vehicle based on unsteady Reynolds-averaged Navier–Stokes equations (RANS) [5]. Compared with the shroud separation of a rocket in outer space, the shroud separation of a hypersonic vehicle in the low-altitude near space is very complex. The high dynamic pressure flow and changes in the aerodynamic shape of the vehicle could create strong shock wave/vortex/turbulent boundary layer interactions [15,16] which makes the flow field highly nonlinear and unsteady, thus seriously affecting the aerodynamic and kinematic characteristics of the vehicle. The shroud separation is one of the high-risk actions in the flight mission of a hypersonic vehicle. However, the flow characteristics and multi-body interaction mechanisms of shroud separation in low-altitude near space are still unclear, and a detailed analysis of the shroud separation process is required.

Table 2. Research status of shroud separation.

Researchers	Theme	Conditions
Guthrie	structural analysis	outer space
Zaitsev	structural analysis	outer space
Whalley	overall design	outer space
Tsutsumi	flow analysis	Mach = 0.8, Re = 2.66 × 10^6
Dagan	flow analysis	Mach = 1.1–2.5
Chamberlain	aerodynamic analysis	Mach = 8.0, Euler method
Raj	kinematic analysis	test conditions: 0.6–0.7
Holden	kinematic analysis	Mach = 3.5–6.0
Wang	flow and kinematic analysis	Mach = 6.0, altitude = 26.0 km, RANS

In this paper, the unsteady multi-body separation characteristics and flow characteristics of hypersonic shroud separation at Mach 7.0 are investigated based on numerical simulation. The improved delayed detached eddy simulation (IDDES) method, dynamic hybrid overset mesh method, and HLLE++ numerical scheme are utilized to ensure numerical accuracy. The results of this study could provide a reference for the design of near-space hypersonic vehicles. The rest of the paper is organized as follows: the research model is described in Section 2, the numerical method and validation are presented in Section 3, the simulation results of shroud separation are presented and discussed in detail in Section 4, and finally, conclusions are presented in Section 5.

2. Model Description

2.1. Models of Vehicle and Shroud

The research model in this study is a simplified model of the hypersonic THAAD (America) vehicle [17], and the maximum flying speed of the hypersonic vehicle is Mach 8.2. The shroud must be dropped in time so that the vehicle can work normally and complete its works when the vehicle arrives at a certain area. The simplification process is presented in Figure 2, and the simplified model is a generic axisymmetric model. The detailed research model in this study is presented in Figures 3 and 4, which is quite simple and is used to investigate the shroud separation of hypersonic vehicles in this paper. The model is designed with an exponential curve because of its high lift-drag ratio in hypersonic speed and the equation for the outer mold line (OML) could be described as:

$$y = 185 \cdot \left(\frac{x}{2326}\right)^{\frac{3}{4}} \tag{1}$$

where x is the axial displacement and y is the radius of the model. As shown in Figures 3 and 4, the origin of the coordinates is located in the head of the shroud. The shroud is comprised of two halves, the upper shroud and the lower shroud, which are split at the symmetrical plane.

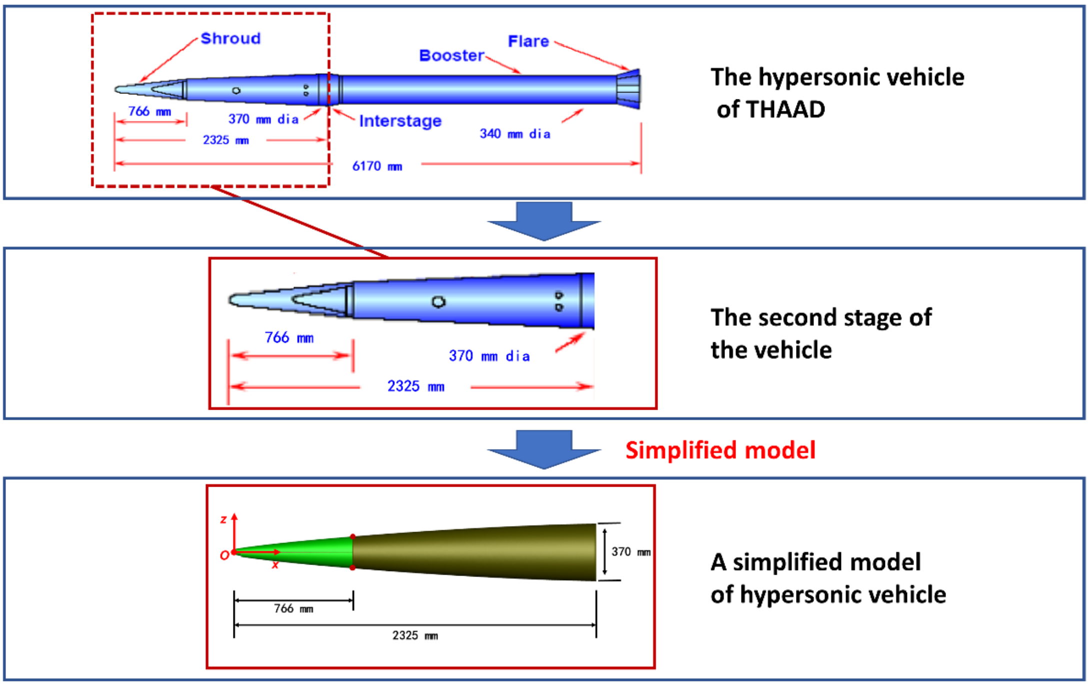

Figure 2. Simplified model of the hypersonic THAAD vehicle.

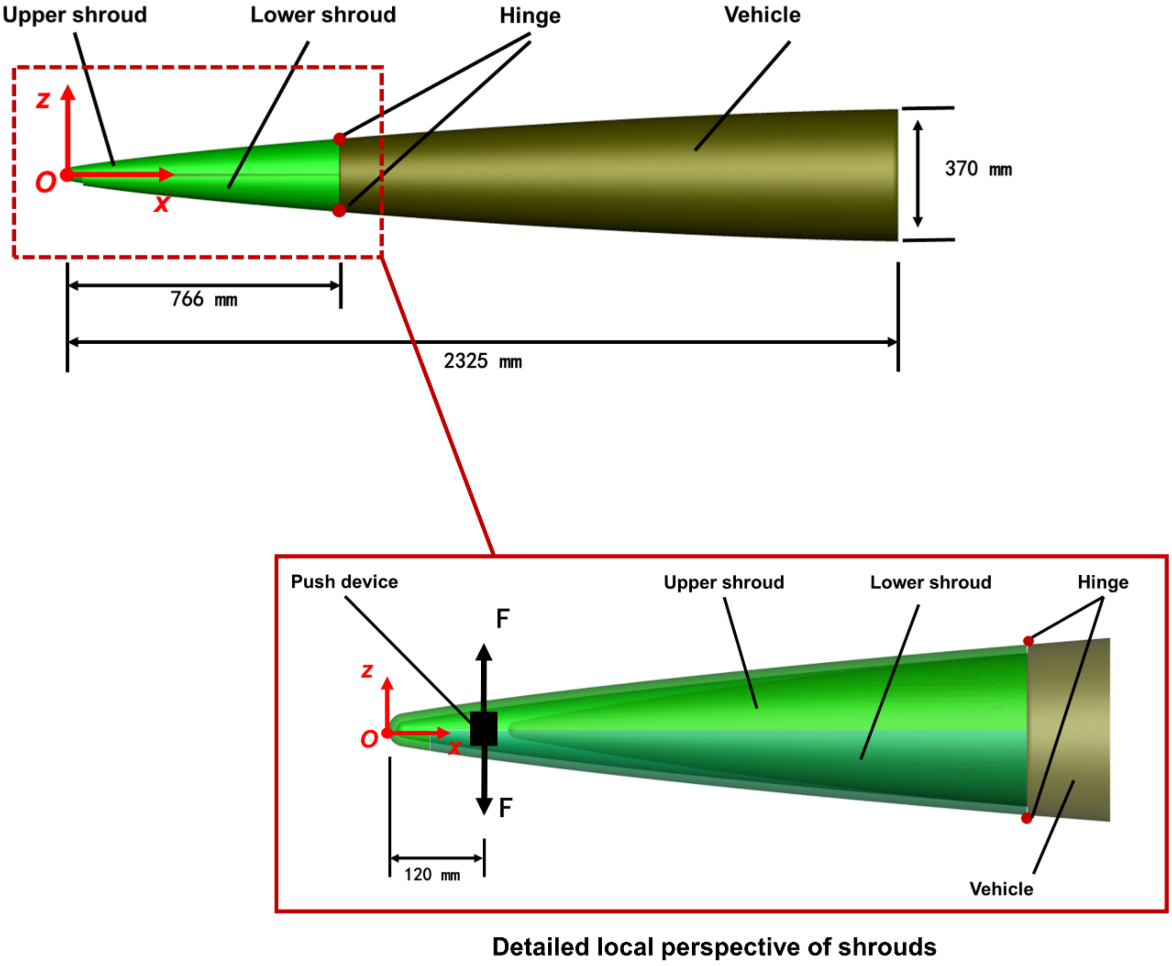

Figure 3. Basic configuration and major dimensions of the research model.

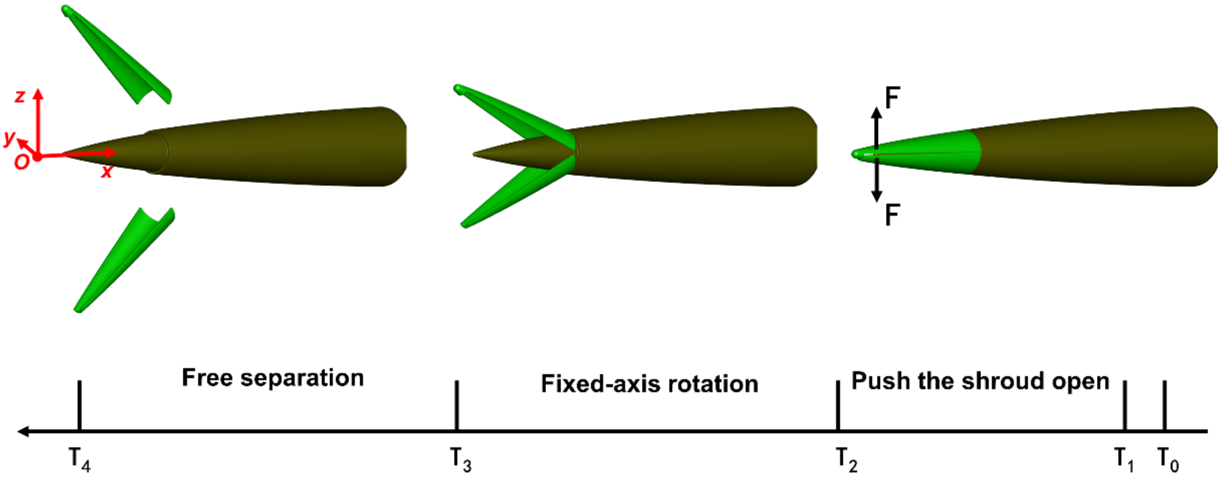

Figure 4. Schematic diagram of the shroud separation process.

It is worth noting from Figure 3 that the upper shroud and the lower shroud are not completely symmetrical, the upper shroud contains a nose cone. The stagnation point in the head of a hypersonic vehicle usually suffers the highest aerodynamic force and heat. If the shroud is split symmetrically, there would be a slit near the stagnation point, which is a serious threat to the safety of the structure of the shroud, so in practice, the shroud is usually split asymmetrically to keep the structural integrity of the head of the shroud. There is a hinge at the rear of each shroud, and each shroud rotates around the fixed hinge axis aligned in the y direction at the beginning of separation. The physical properties of the shrouds and vehicle are presented in Table 3, including the mass, coordinates of the mass center point, and the moment of inertia with respect to the mass center.

Table 3. Physical properties of the shrouds and vehicle.

	Mass (kg)	Coordinates of the Mass Center Point (m)	Moment of Inertia with Respect to the Mass Center (kg·m^2)
upper shroud	12.677	x = 0.4649 y = 0.0 z = 0.0432	I_{xx} = 0.0390 I_{yy} = 0.5393 I_{zz} = 0.5656
lower shroud	12.230	x = 0.4801 y = 0.0 z = -0.0447	I_{xx} = 0.0386 I_{yy} = 0.4538 I_{zz} = 0.4802
vehicle	1076.550	x = 1.6089 y = 0.0 z = 0.0	I_{xx} = 13.1866 I_{yy} = 273.4137 I_{zz} = 273.4137

2.2. Process of Hypersonic Shroud Separation

Table 4 lists the free-stream flow conditions of the hypersonic shroud separation in this paper, which is a typical example of hypersonic vehicles' real flight in near space and has the characteristics of a high dynamic pressure and dense atmosphere. The time of hypersonic shroud separation is very short (often within 100 ms), therefore, the shroud is treated as a rigid body in this study. Figure 4 presents the process of shroud separation, which could be described as follows:

Table 4. Free-stream flow conditions of shroud separation.

P_∞	T_∞	Altitude	Mach	Attack Angle	Sideslip Angle
2549.22 Pa	221.552 K	25 km	7.0	0	0

T0: Start. The shroud receives a command to separate.

T1~T2: The shrouds are pushed open. As presented in Figure 3, there is a push device in the front of the shrouds, which is 120 mm from the head. Both the shrouds are driven to move by the push device, and the upper and lower shroud are pushed to open a short distance. T1 is the time when the push device starts to work, and T2 is the time when the push device ends the work. The push device provides a gradually decreasing force F, which could be described as:

$$F = \begin{cases} 5000 \times (z_F - z_{F\max}) \\ 0 : z_F > z_{F\max} \qquad\qquad z_{F\max} = 0.03m \end{cases} \tag{2}$$

where the unit of F is the Newton (N), z_F is the displacement of the force point, and z_{Fmax} is the maximum action distance of F. When z_F is larger than z_{Fmax}, the push device can no longer provide any force to the shrouds and the shrouds will separate due to the large aerodynamic forces.

T2~T3: Fixed-axis rotation. At the beginning of separation, the shrouds are locked with the vehicle by a hinge. The high dynamic pressure flow impacts the inside of the shroud and creates large aerodynamic forces which drive each shroud to rotate around the fixed hinge to an unlocking angle. T3 is the time when the shroud unlocks with the vehicle; the unlocking angle is 30 degrees in this study.

T3~T4: Free separation. The shrouds unlock with the vehicle at a pitch angle of 30 degrees and then separate freely, driven by the aerodynamic forces. T4 is the time when the shroud and vehicle no longer interact with each other and finish the shroud separation.

3. Numerical Method and Validation

First, the numerical method is presented in Section 3.1, including the FlowStar flow solver, IDDES method, HLLE++ numerical scheme, and time-stepping strategy. The shroud separation of the hypersonic vehicle in the low-altitude near space is very complex. The high dynamic pressure flow and changes in the aerodynamic shape of the vehicle could create strong shock wave/vortex/turbulent boundary layer interactions, and the IDDES method could provide the details of the complex flow field. The newly developed HLLE++ numerical scheme has low numerical dissipation and could capture flow characteristics such as shock waves, shear layers, and vortexes well. Second, the mesh generation is described in Section 3.2. The dynamic hybrid overset mesh method is utilized to simulate the shroud separation, and the grid area where the shroud may pass through is especially refined. Finally, the validation and verification are presented in Section 3.3, including mesh independency verification, time independency verification, IDDES method verification, and wind tunnel experiment validation of hypersonic multi-bodies separation.

3.1. Numerical Method

3.1.1. Software and Governing Equation

FlowStar flow solver, which is a self-developed flow solver of computational fluid dynamics (CFD) by China Aerodynamics Research and Development Center (CARDC), was used to simulate the shroud separation in this study [18–21]. The flow solver was developed based on large-scale parallel-computing technology and the unstructured finite volume method, and an unsteady simulation and grid adaptation are its characteristics. FlowStar combines the dynamic hybrid overset mesh method and six-degrees-of-freedom (6DOF) motion to simulate the multi-body separation motions, such as shroud separation, store releasing, propeller slipstream, stage separation, and shroud separation of the aircraft. The feature-based grid-adaptation method [18,22,23] and adjoint-based grid-adaptation method [24,25] were developed to provide accurate aerodynamic characteristics and flow characteristics.

The unsteady governing equation was used:

$$\frac{\partial}{\partial t}\iiint\limits_{\Omega} \boldsymbol{Q} dV + \oiint_{\partial\Omega}\left(\boldsymbol{H}(\boldsymbol{Q})\cdot\vec{\boldsymbol{n}} - \boldsymbol{Q}\vec{\boldsymbol{v}}_g.\vec{\boldsymbol{n}}\right)dS = \oiint_{\partial\Omega}\boldsymbol{H}_v(\boldsymbol{Q})\cdot\vec{\boldsymbol{n}}dS \tag{3}$$

where Ω denotes the volume of the control volume, $\boldsymbol{Q}$ denotes the conservative state vector, $\vec{\boldsymbol{v}}_g$ denotes the wall velocity, $\vec{\boldsymbol{n}}$ denotes the outward-pointing normal unit vector, $\boldsymbol{H}(\boldsymbol{Q})$ denotes the inviscid flux vector, and $\boldsymbol{H}_v(\boldsymbol{Q})$ denotes the viscous flux vector. The flux vector and conservative-state vector can be described as:

$$\begin{gathered}\boldsymbol{Q} = \begin{bmatrix}\rho & \rho u & \rho v & \rho w & \rho E\end{bmatrix}^{\mathrm{T}} \\ \boldsymbol{H}(\boldsymbol{Q}) = \begin{bmatrix}\rho V \\ \rho u V + p n_x \\ \rho v V + p n_y \\ \rho w V + p n_z \\ \rho H V\end{bmatrix} \quad \boldsymbol{H}_v(\boldsymbol{Q}) = \begin{bmatrix}0 \\ n_x\tau_{xx} + n_y\tau_{xy} + n_z\tau_{xz} \\ n_x\tau_{yx} + n_y\tau_{yy} + n_z\tau_{yz} \\ n_x\tau_{zx} + n_y\tau_{zy} + n_z\tau_{zz} \\ n_x\Theta_x + n_y\Theta_y + n_z\Theta_z\end{bmatrix}\end{gathered} \tag{4}$$

where ρ denotes the density; u, v, and w denote the velocities in three directions; E denotes the total energy; V denotes the contravariant velocity; p denotes the pressure; and τ denotes the viscous stress.

The inviscid flux was discretized with the HLLE++ scheme, which is introduced in detail in Section 3.1.3, and the viscous term was discretized by the central difference scheme. A Venkatakrishnan limiter was used to restrict numerical oscillation [26], which can be described as:

$$\Psi_i = \min_j\begin{cases}\min(1, \dfrac{(d_{\max})^2 + \varepsilon^2 + 2d_f\cdot d_{\max}}{(d_{\max})^2 + \varepsilon^2 + 2(d_f)^2 + d_f\cdot d_{\max}}) & d_f > 0 \\ \min(1, \dfrac{(d_{\min})^2 + \varepsilon^2 + 2d_f\cdot d_{\min}}{(d_{\min})^2 + \varepsilon^2 + 2(d_f)^2 + d_f\cdot d_{\min}}) & d_f < 0 \\ 1 & d_f = 0\end{cases} \tag{5}$$

and the coefficients can be described as:

$$\begin{aligned} d_f &= \nabla q\cdot(\vec{r}_{fc_j} - \vec{r}_{cc}) \\ d_{\max} &= \max(\max(q_j), q_i) - q_i \\ d_{\min} &= \min(\min(q_j), q_i) - q_i \end{aligned} \tag{6}$$

where ∇q denotes the gradient, q_i and q_j denote the flow variables of the left face and right face, respectively.

3.1.2. IDDES Method

The detached eddy-simulation (DES) method utilizes the Reynolds-averaged Navier–Stokes equations (RANS) to solve the thin boundary-layer area and uses the large-eddy-simulation (LES) method to solve the other areas, which is essentially a hybrid method of the LES and RANS [27,28]. The DES method combines the advantages of LES and RANS and could be utilized to simulate the highly unsteady separation flow. However, when the original DES method is used to solve the thick boundary layer, the flow would separate too early, which would result in an incorrect flow field. Therefore, the delayed detached-eddy-simulation (DDES) method and IDDES method were proposed to solve this problem [29,30]. In the IDDES method, the LES length scale for anisotropic grids near the wall is modified, which makes use of the wall distance along with the grid spacing. In addition, the blending of RANS and LES behavior within the wall-modeled large-eddy simulation (WMLES) is modified, which greatly increases the resolved turbulence activity near the wall, and finely adjusts the resolved logarithmic layer. The shear-stress-transport (SST) turbulence model is used in the prediction of the IDDES method in this paper.

The length scale in the IDDES method is described as:

$$\Delta = \min\{\max[0.15d_w, 0.15h_{\max}, l_w], h_{\max}\} \tag{7}$$

where $h_{\max} = \max(\Delta_x, \Delta_y, \Delta_z)$, Δ_x, Δ_y, and Δ_z are the grid scale in the three coordinate directions; l_w is the length of the grid in the direction perpendicular to the wall; and d_w is the distance to the nearest wall.

The IDDES method blends RANS and LES as:

$$l_{IDDES} = f'_d(1 + f_e)l_{RANS} + (1 - f'_d)l_{WMLES} \tag{8}$$

where l_{RANS} is the RANS length scale, l_{WMLES} is the WMLES length scale, f_e is the correction coefficient, and other coefficients can be described as:

$$\begin{aligned}
f_d &= 1 - \tanh\left([C_d r'_d]^3\right) \\
f'_d &= \max\{(1 - f_d), f_B\} \\
f_B &= \min\{2\exp(-9\alpha^2), 1.0\} \\
\alpha &= 0.25 - \frac{d_w}{h_{\max}} \\
r'_d &= \frac{v_t}{\sqrt{U_{i,j}U_{i,j}}\kappa^2 d^2}
\end{aligned} \tag{9}$$

3.1.3. HLLE++ Scheme

The numerical scheme is the soul and foundation of numerical simulation. There is a complex flow field of shock wave/vortex/turbulent boundary layer interaction during the hypersonic shroud separation in the low-altitude near space, which requires a low dissipative numerical scheme that could accurately capture the shock waves and vortexes. Some approximate Riemann schemes, such as the HLLC scheme and Roe scheme, are highly sensitive to how well the grids are aligned with the shocks. When the grids are not aligned with the shock waves, cross-coupling between the Riemann problems in the different directions occurs, and the flow field quality would be severely degraded, resulting in non-physical features, which are often called "carbuncles" [31]. The HLLE++ scheme utilizes a pressure-gradient-based switching function to locally transition to a more robust algorithm in the vicinity of strong shocks, and it removes errors in the vicinity of non-grid-aligned shocks. The HLLE++ scheme could produce almost grid-independent solutions regardless of grid alignment with strong shocks.

The HLLE++ scheme is a newly developed method, and many CFD softwares, such as OVERFLOW [31], FlowStar [32,33], Kestrel, and KCFD [34,35], have developed this scheme. It has been shown that the HLLE++ scheme provides significantly better solutions than the original Roe and HLLC schemes for the flow fields with strong shocks, vortexes, and shear layers, and it is suitable for the numerical simulation of hypersonic shroud separation.

The eigenvalue of the HLLE++ scheme is defined as:

$$\lambda^{HLLE++} = \beta\lambda^{HLLE+} + (1 - \beta)\lambda^D \tag{10}$$

where λ^{HLLE+} is the eigenvalue of HLLE+, λ^D is the eigenvalue of the dissipative term, and β is the switching function, which can be defined as:

$$\beta = 1 - \tanh\left(\frac{\max(k_p, 75) - 75}{100}\right) \tag{11}$$

where k_p is a pressure-gradient-based switch sensor:

$$k_p = 35\frac{\vec{V}}{c} \cdot \frac{\nabla p}{p}\Omega^{\frac{1}{3}} \tag{12}$$

The switch is only activated where there are strong shocks and does not affect other areas of the flow such as boundary layers. Therefore, The HLLE++ scheme could capture hypersonic shocks without encountering the "carbuncle" phenomena occurring and without corrupting the low numerical dissipation of the scheme in boundary layers.

3.1.4. Time Stepping

Dual time-stepping is used for time-stepping, and the Lower Upper-Symmetric Gauss–Seidel (LU-SGS) is used to solve the governing equation [36]. The discrete governing equation is divided into three parts in the LU-SGS method:

$$(D + L)D^{-1}(D + U)\Delta\vec{W}^{n} = -\vec{R}_I^{n} \tag{13}$$

where D is a diagonal matrix, L is a strictly lower triangular matrix, and U is a strictly upper triangular matrix. Equation (13) can be solved with a forward sweep and a backward sweep:

$$\begin{aligned} (D + L)\Delta\vec{W}^{(1)} &= -\vec{R}_I^{n} \\ (D + U)\Delta\vec{W}^{n} &= D\Delta\vec{W}_I^{(1)} \end{aligned} \tag{14}$$

The LU-SGS method is widely used because it is relatively simple to execute and has a low memory requirement.

3.2. Mesh Generation

3.2.1. Conservative Overset Mesh Method

The dynamic hybrid overset mesh method is the most popular method to simulate multi-bodies separation, and it is used for the simulation of the shroud separation in this study. The complex flow area is divided into many independent sub-areas in the overset mesh method, and the mesh of each area is generated independently. The flow field of each mesh is also calculated independently, and the flow field information of each mesh is transferred in the overlapping areas.

The overset mesh needs to eliminate the cells that do not participate in the simulation, which is also called "hole-cutting". A "direct cutting" method is used in FlowStar flow solver, which utilizes the solid surface intersection criterion to determine the hole boundary [18,37] (Figure 5). The "direct cutting" method does not require auxiliary mesh and could provide high robustness and efficiency.

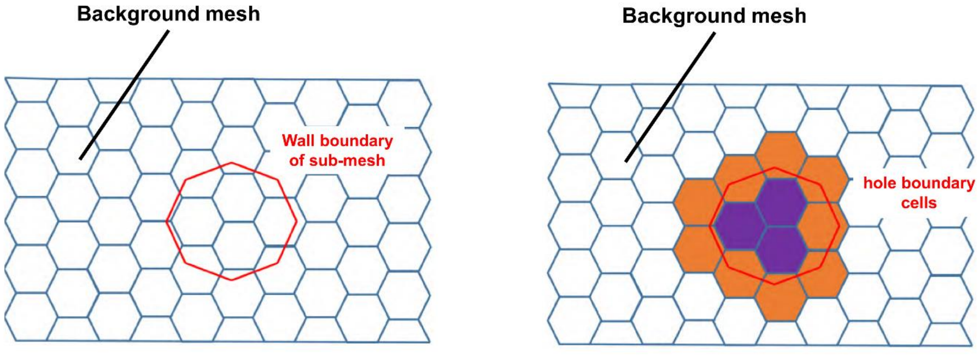

(**a**) (**b**)

Figure 5. Schematic diagram of the overset assembly based on the "direct cutting" strategy: (**a**) two overset sub-meshes; (**b**) direct cutting technique.

The data transfer between overlapping grids is the basis for ensuring the correct calculation, especially for the hypersonic flow field with strong shocks. A conservative data transfer method, based on the super mesh technology and the center-based finite volume method, is used in FlowStar flow solver, which could ensure the conservation and accuracy of the overset mesh method [38].

3.2.2. Mesh Generation for Shroud Separation

A reasonable design and high-quality generation of computational mesh are prerequisites for the numerical simulation of the shroud separation. Dynamic hybrid overset mesh is used in this paper, hexahedrons and triangular prisms are used in the boundary layer to better simulate the viscous flow, tetrahedrons are used for the simulation of the spatial flow field, and pyramid elements are utilized for the transition between hexahedrons, prisms, and tetrahedrons.

Figures 6 and 7 present the overset mesh of shroud separation, which contains three sub-meshes: the mesh of the vehicle, the mesh of the upper shroud, and the mesh of the lower shroud. Figure 7 presents the grid distribution of the shroud separation area; it can be seen that the grid areas where the shroud may pass through are especially locally refined. The local refinement of grids provides two benefits, on the one hand, the reasonable grid size of the overlapping area could ensure the accuracy of overset mesh, on the other hand, the flow features, such as shock waves, vortexes, and boundary layers, could be well captured.

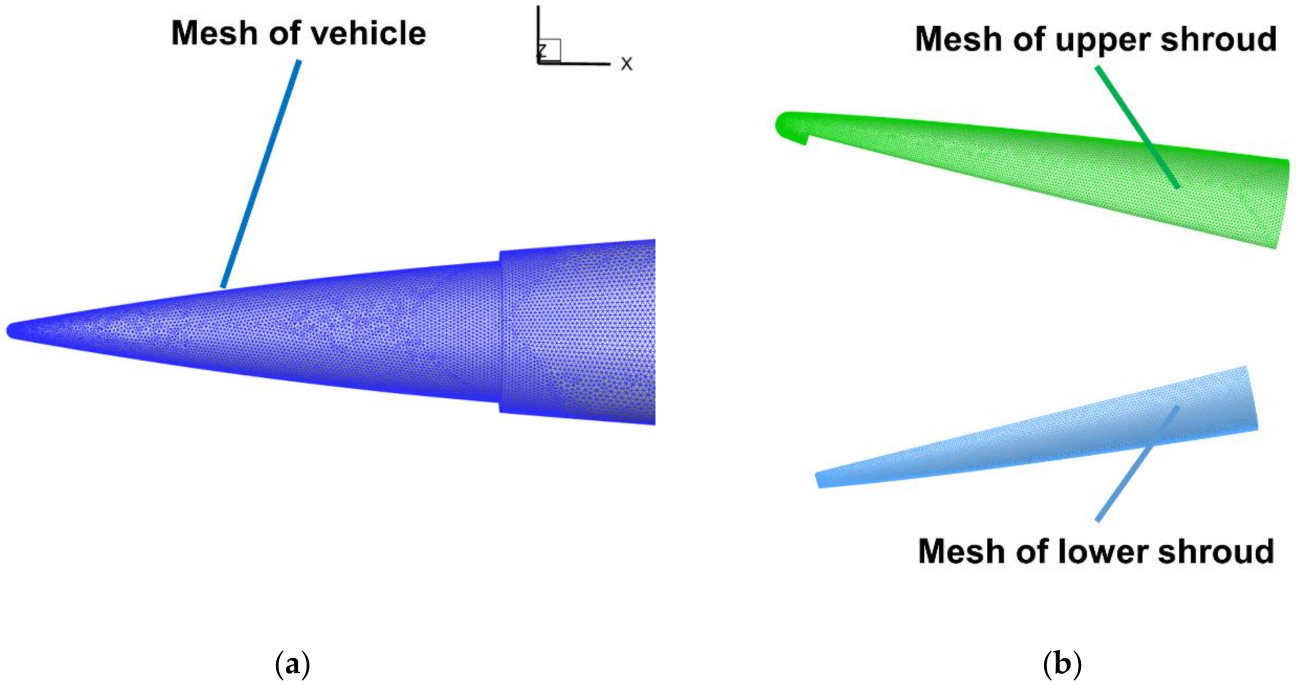

Figure 6. The surface mesh of the vehicle and shrouds: (**a**) surface mesh of the vehicle; (**b**) surface mesh of the shrouds.

The number of grid elements in the vehicle is about 38 million, the number of the grid elements of the upper shroud and lower shroud is about 4 million, and the number of total grid elements is about 46 million. The grid scale of the first layer is 0.000004 m, according to the criterion of $y+ < 1$. Mesh independency will be studied in the next section.

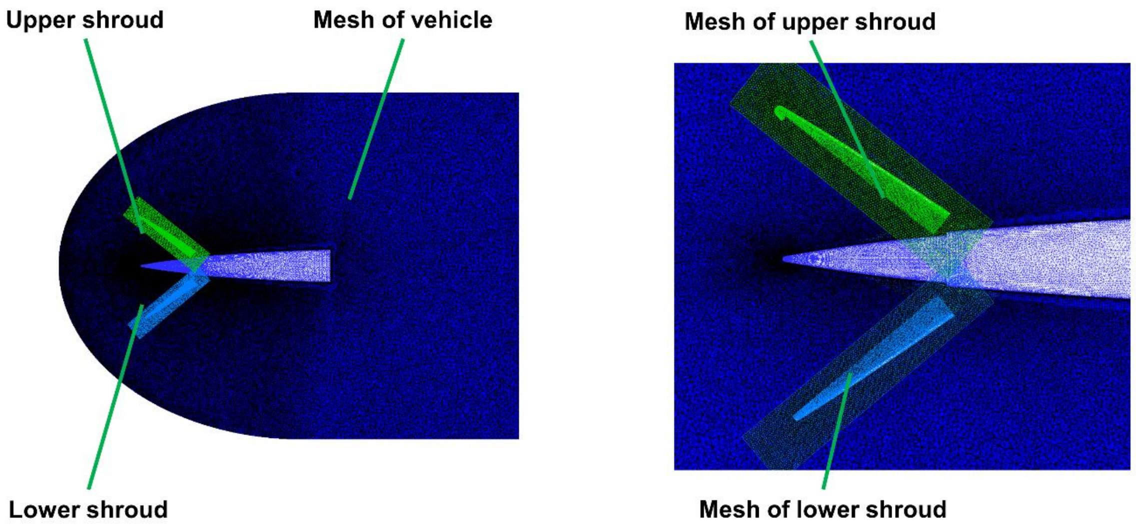

(**a**) (**b**)

Figure 7. The overset mesh of shroud separation: (**a**) the three sub-meshes of shroud separation; (**b**) the grid distribution of the separation area.

3.3. Verifications and Validations

3.3.1. Mesh Independency Verification

Three different sets of hybrid overset meshes, coarse mesh, medium mesh, and fine mesh, are built to verify the mesh independency. The meshes are different in the grid scale of surface and space. The number of total elements of the coarse mesh is about 31.0 million, the number of total elements of the medium mesh is about 46.0 million, and the number of total elements of the fine mesh is about 65.4 million.

The three different sets of hybrid overset meshes are utilized to simulate the shroud separation, and the pitch angle of the upper shroud during the separation process is presented in Figure 8. It can be seen that the trends of the three curves are consistent, however, the result of the coarse mesh deviates from the results of the medium mesh and fine mesh, and the cumulative error becomes larger and larger with increasing time. The separation characteristics of the medium mesh and the fine mesh are almost the same. In consideration of the accuracy and cost of the numerical simulation, the medium mesh (46 million) is used in this study.

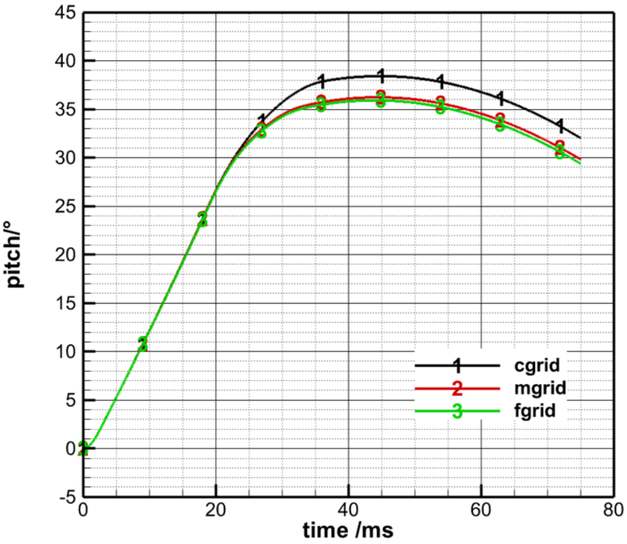

Figure 8. Mesh independency verification.

3.3.2. Time Independency Verification

To ensure that the numerical results are independent of the time step in the unsteady simulation, three different time steps are set to verify the time independency: 0.05 ms (long time step), 0.01 ms (medium time step), and 0.002 ms (short time step). The three different time steps are utilized to simulate the shroud separation, and the pitch angle of the upper shroud during the separation process is presented in Figure 9. It can be seen that the result of the long time step clearly deviates from the results of the medium time step and short time step, while the results of the medium time step and short time step are almost the same. There would be many numerical cases of shroud separation, therefore, in consideration of the accuracy and cost of the numerical simulation, the medium time step (0.01 ms) is used in the simulation of shroud separation.

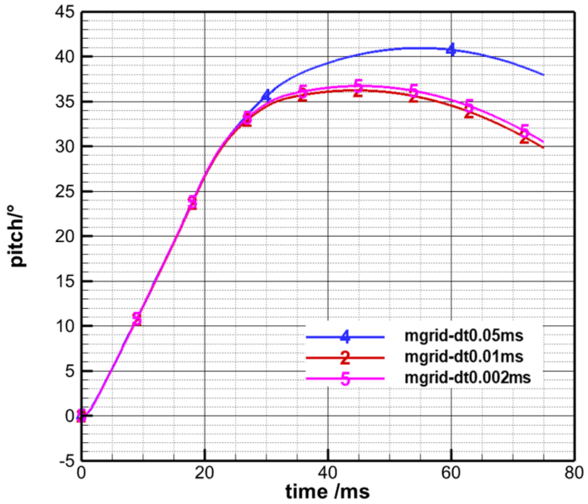

Figure 9. Time independency verification.

3.3.3. IDDES Method Verification

The M219 cavity is a benchmark widely used in the numerical verification of DES-type methods, and there is a large number of reliable experimental data and numerical data on the M219 cavity [39,40]. The M219 cavity was used to verify the IDDES method in this study. The details of the configuration of the M219 cavity are presented in Refs. [41,42]. There are 10 monitoring points at the bottom of the cavity to monitor the pressure fluctuation (Figure 10). The grid scale of the first layer is 0.000002 m, according to the criterion of y+ < 1, the time step in unsteady simulation is 0.01 ms, and the free-stream flow conditions of the numerical simulation are the same as the wind-tunnel experiments [43].

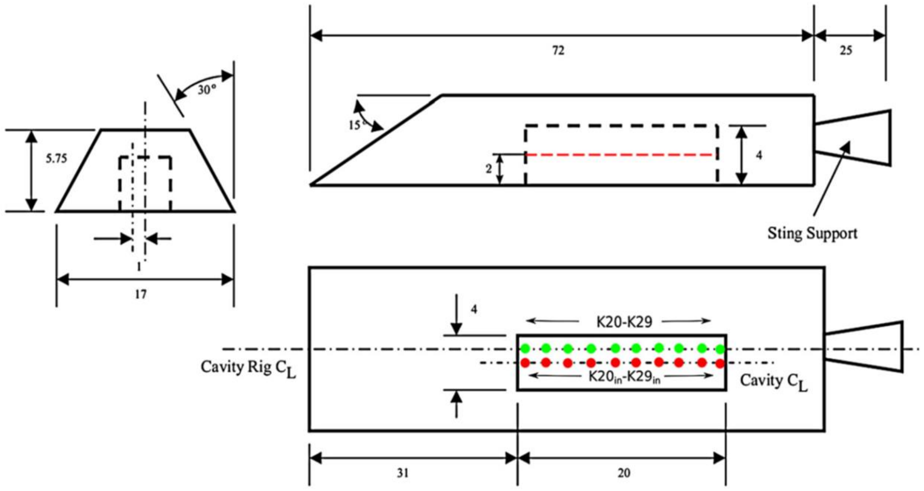

Figure 10. The geometry of the M219 cavity.

The numerical results of this study were compared with the results of wind-tunnel experiments. Figure 11 presents the overall sound-pressure level (OASPL) at the bottom floor, and Figure 12 presents the sound-pressure levels of each monitoring point. It can be seen that the CFD results are in good agreement with the wind-tunnel experiments.

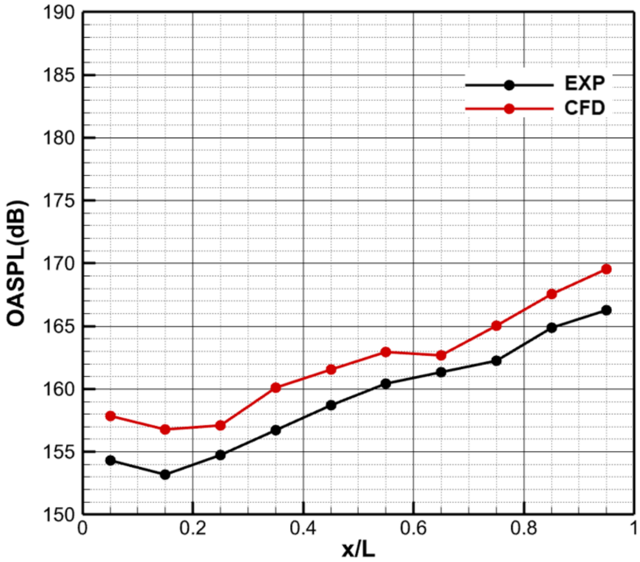

Figure 11. Overall sound-pressure level (OASPL) [43].

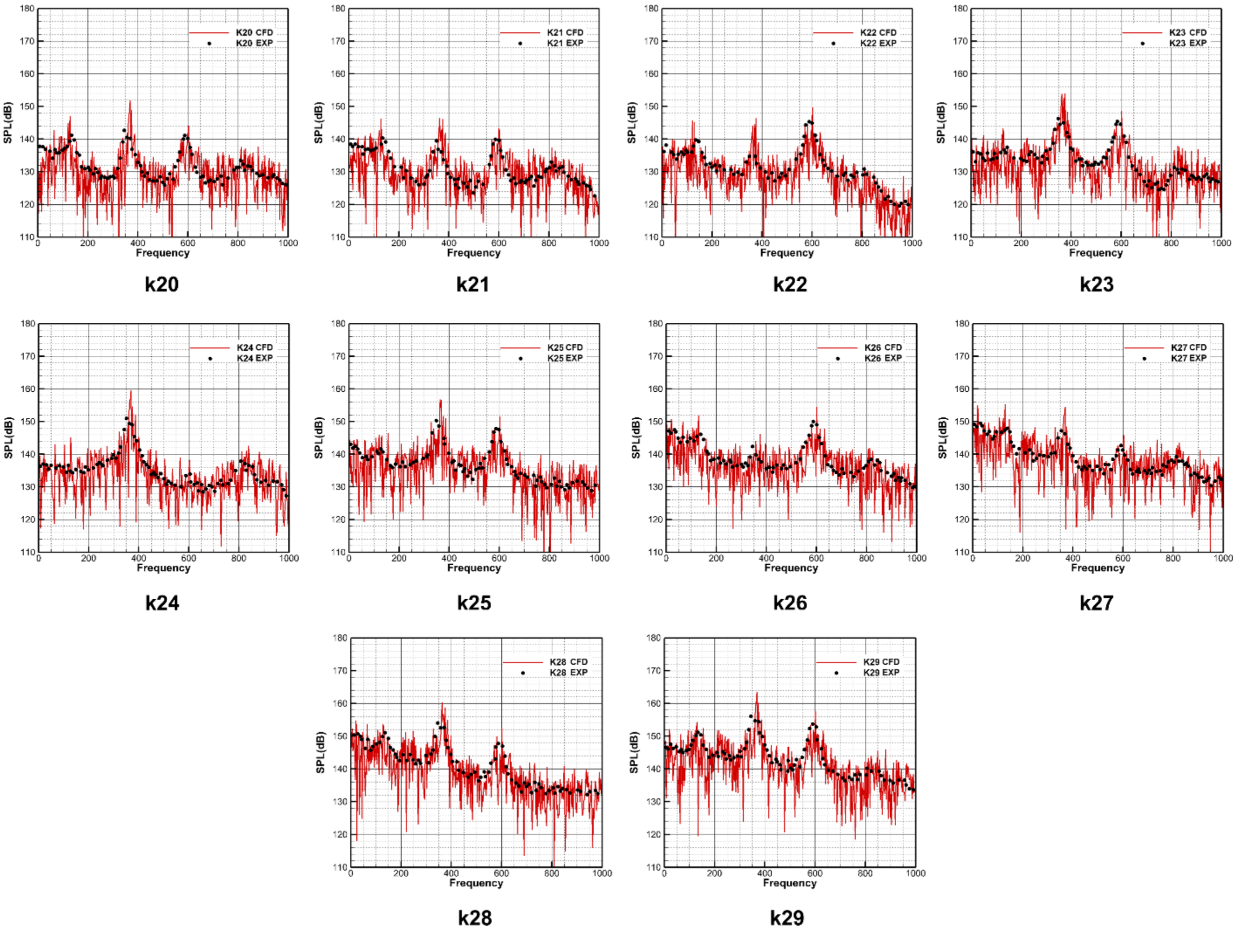

k20 k21 k22 k23

k24 k25 k26 k27

k28 k29

Figure 12. Sound-pressure levels (SPL) at the monitoring points [43].

3.3.4. Validation of the Numerical Method of Hypersonic Multi-Bodies Separation

It is very difficult to find benchmarks of hypersonic shroud separation in public papers. Therefore, a captive trajectory system (CTS) wind tunnel experiment of hypersonic stage separation is used to verify the numerical method of multi-body separation in this study. The model of stage separation is described in detail in reference [44] (Figure 13). The wind tunnel experiment is performed in the 1 m hypersonic wind tunnel in CARDC, and free-stream flow conditions are listed in Table 5, where P_0 is total pressure and q_∞ is dynamic pressure. Figure 13a shows the location of the first stage and second stage in the wind tunnel; the models are driven by a 6-DOF mechanism. Although the flow conditions and geometry of the wind tunnel experiment are different from the shroud separation in this study, it is a good example to verify the numerical method of hypersonic multi-body separation in this study.

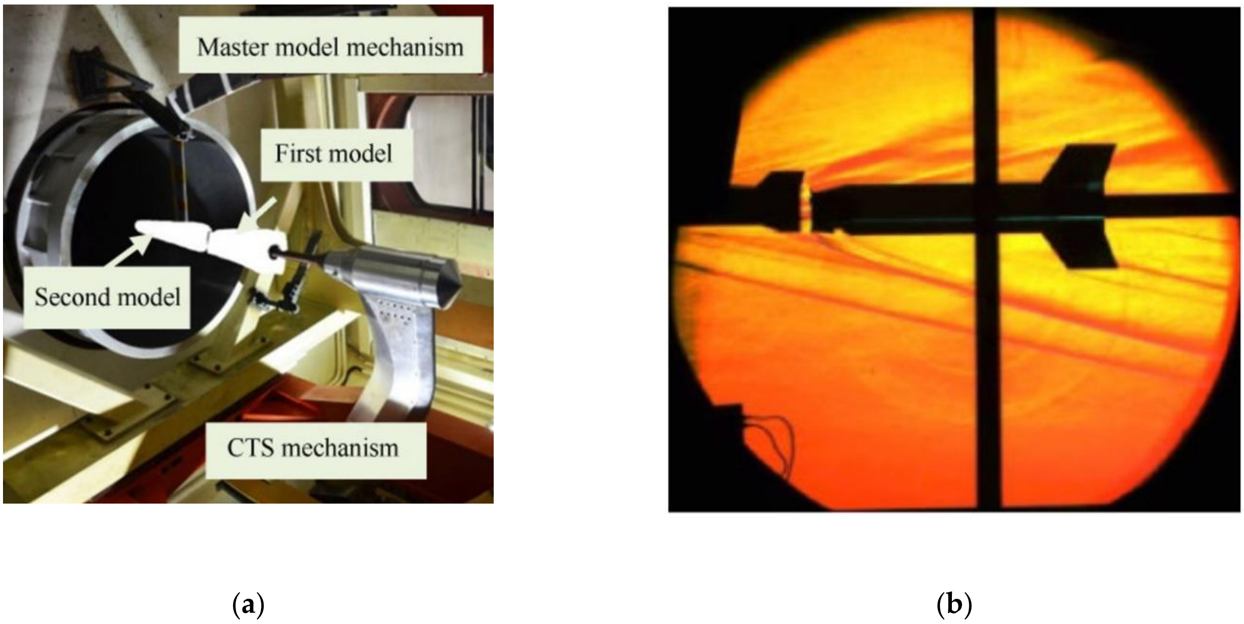

(**a**) (**b**)

Figure 13. Wind tunnel experiment of hypersonic stage separation: (**a**) model and mechanism in the wind tunnel; (**b**) Schlieren images of wind tunnel experiment [44].

Table 5. Free-stream flow conditions of stage separation.

P_0/kPa	T_∞/K	P_∞/kPa	Mach	q_∞/kPa
1349	360	2.549	5.0	44.6

The flow conditions of numerical simulation are the same as the wind tunnel experiment, and the comparison between the numerical simulation and wind tunnel experiment is presented in Figure 14. It can be seen that the CFD results are in good agreement with the wind tunnel experiments, which indicates that the numerical method of multi-body separation in this paper is suitable for the hypersonic multi-body separation.

In summary, the numerical method has been fully validated, including mesh independency verification, time independency verification, IDDES method verification, and wind tunnel experiment validation of hypersonic multi-bodies separation, indicating that the numerical method in this paper is suitable for the hypersonic shroud separation.

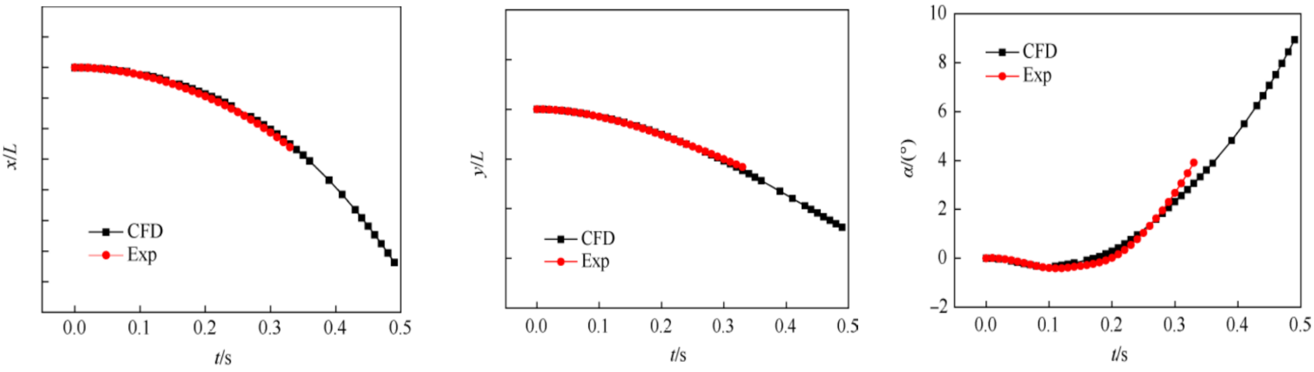

(**a**) (**b**) (**c**)

Figure 14. Comparison between numerical simulation and wind tunnel test: (**a**) x-direction distance; (**b**) y-direction distance; (**c**) pitch angle. [44].

4. Results and Discussion

4.1. Multi-Body Separation Characteristics

The free-stream flow conditions of the hypersonic shroud separation are listed in Table 4, the multi-body separation characteristics of the shroud are presented in Figure 15, and the trajectory of the shrouds during the separation is presented in Figure 16. It can be seen that the upper shroud and lower shroud gradually move away from the vehicle and are successfully separate from the vehicle. At T = 0 ms, the shrouds receive a command to separate. Then, the push device in the front of the shroud starts working, and the upper shroud and lower shroud are pushed to open a short distance. At T = 3.24 ms, the force of the push device decreases to 0. The high dynamic pressure flow impacts the inside of the shrouds and creates large aerodynamic forces which drive each shroud to rotate around the fixed hinge to 30 degrees. It can be seen from Figure 16b the that upper shroud and lower shroud show a slight asymmetry during separation, which is caused by the asymmetric configuration of the upper shroud and lower shroud, i.e., the upper shroud contains a nose cone. The lower shroud first reaches the unlocking angle and unlocks with the vehicle at T = 20.94 ms. The upper shroud also reaches the unlocking angle and unlocks with the vehicle at T = 22.96 ms. After unlocking the vehicle, the shrouds separate freely, driven by aerodynamic forces.

The aerodynamic characteristics of the shrouds during the separation process are presented in Figure 17, including the normal force (Fz) and pitch moment. It should be noted that the reference point of the pitch moment is the center of mass of the shroud. Therefore, although the pitch moment is negative, the upper shroud is still in a head-raise motion because of a fixed-axis rotation before unlocking with the vehicle.

It is worth noting from Figure 17 that, within a very small time window from 18.53 ms to 24.05 ms, there is a strong disturbance in the aerodynamic forces of shrouds. At T = 18.53 ms, both the upper shroud and lower shroud are still locked with the vehicle, therefore, the strong disturbance of the aerodynamic characteristics is not caused by the unlocking of the shrouds.

It can be seen from the Mach number contours in Figure 15, from 18.53 ms to 24.05 ms, there is also a strong disturbance in the flow field inside the shrouds. Actually, there is a strong unsteady shock wave/vortex/turbulent boundary layer interaction during the shroud separation, and a detailed discussion is presented in the next section. Additionally, with the increasing opening angle of the shrouds during separation, there is also a strong separation flow on the leeward side of the shroud, which is essentially a flow separation issue at a large attack angle. There is already much detailed and deep research about flow separation in a large attack angle. Therefore, this paper only focuses on the unsteady shock wave/vortex/boundary layer interaction in the flow field inside the shrouds.

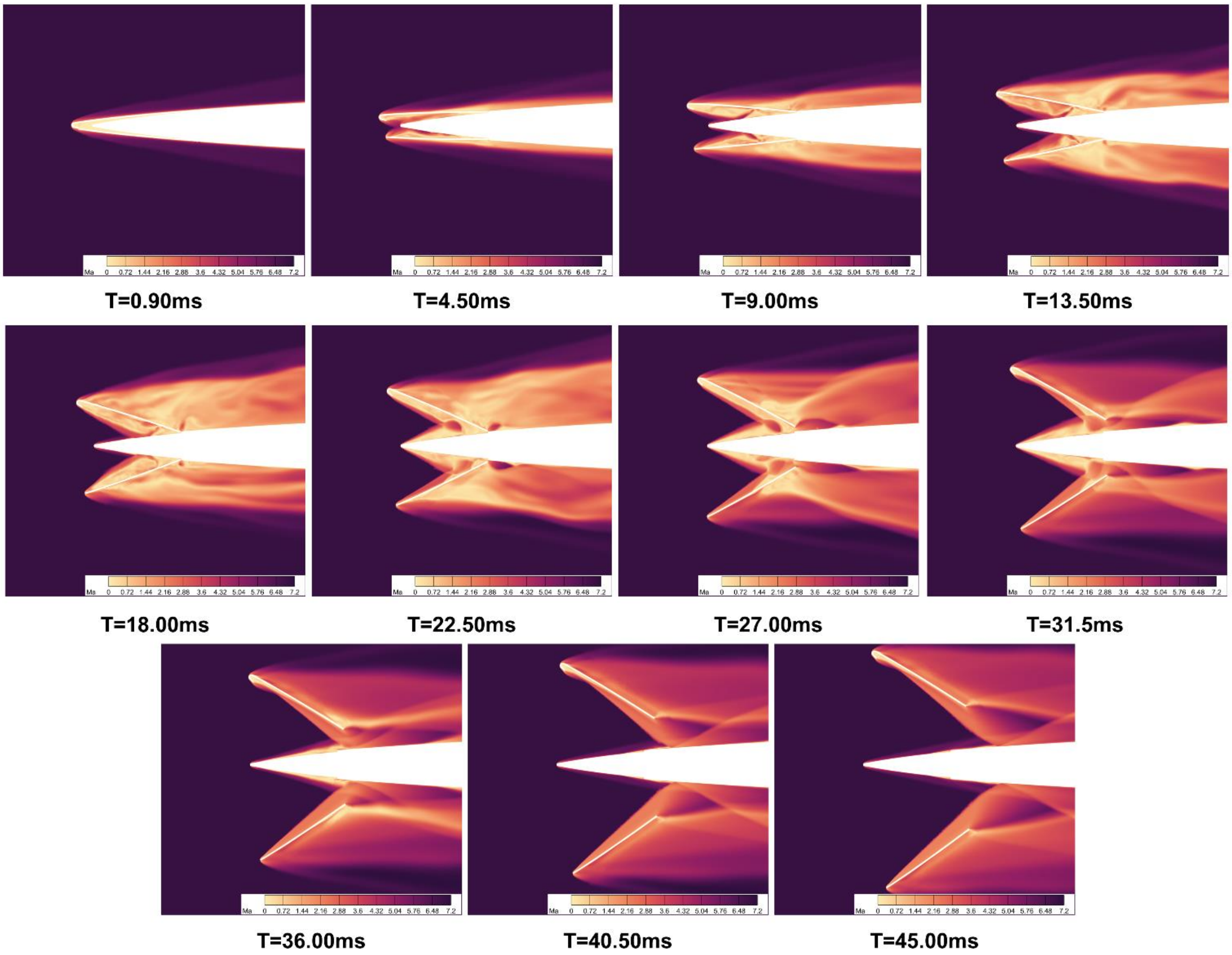

T=0.90ms T=4.50ms T=9.00ms T=13.50ms

T=18.00ms T=22.50ms T=27.00ms T=31.5ms

T=36.00ms T=40.50ms T=45.00ms

Figure 15. Multi-body separation characteristics of the shroud.

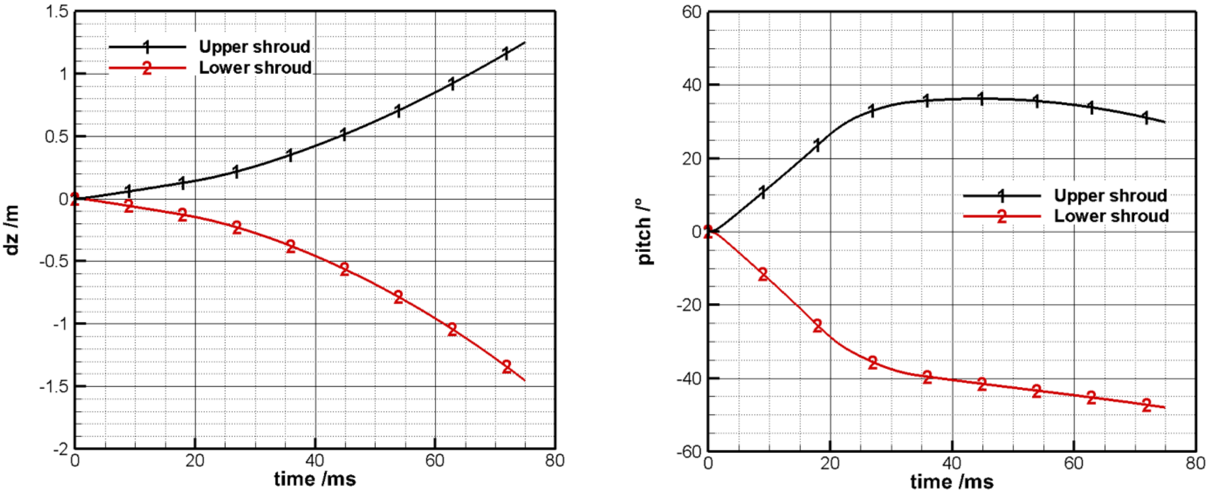

(**a**) (**b**)

Figure 16. The trajectory of the shroud during the separation process: (**a**) z-direction distance; (**b**) pitch angle.

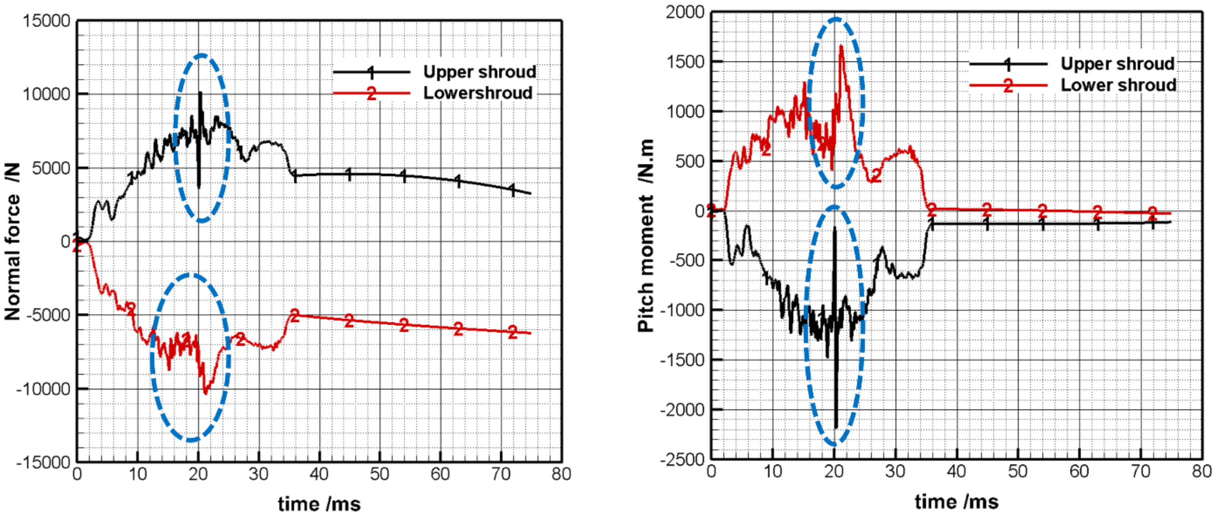

(**a**) (**b**)

Figure 17. Aerodynamic characteristics of the shroud during the separation process: (**a**) normal force (Fz); (**b**) pitch moment. (The blue lines present a strong disturbance in the aerodynamic forces of shrouds.)

4.2. Shock Wave/Vortex/Boundary Layer Interaction

4.2.1. Generation and Expansion of Separation Vortexes

The flow characteristics of shroud separation before T = 18.00 ms are presented in Figures 18–21, including the contour of streamline and Mach number, the iso-surface of Q-criterion, and the contour of pressure coefficient. At T = 0.90 ms, the shrouds are separating under the force of the push device, and the opening angle of the shrouds is still very small, showing a typical hypersonic flow field (Figure 18). At T = 9.00 ms, the opening angles of the upper and lower shroud are 10.77 degrees and 11.63 degrees, respectively, and it can be seen that there is a complex flow field of shock wave/vortex/boundary layer interaction in the area inside the shrouds (Figure 19).

There are three main types of shock waves in the area inside the shrouds:

(1) A-type shock: detached shock. As shown in Figure 22a, the detached shock is caused by the supersonic flow with a blunt body.

(2) B-type shock: separation shock. As shown in Figure 22b, the high dynamic pressure flow impacts the inside of the shrouds and creates a strong adverse pressure gradient, which separates the upstream boundary layer and results in a separation shock wave.

(3) C-type shock: reflected shock. There are many reflected shocks in the area inside the shrouds, for example, as shown in Figure 22c, the separation shock of the shroud impacts the vehicle and produces a reflected shock. The shock wave could be reflected many times between the shroud and the vehicle.

Q-criterion is a common method used to identify and visualize the structure of a spatial vortex, and there are three main types of vortexes in the area inside the shrouds before T = 18.00 ms:

(1) A-type vortex: the vortex caused by a blocking effect. As shown in Figure 22b, the generation mechanism of an A-type vortex is the same as separation shock, the high dynamic pressure flow is blocked by the shroud and creates a strong adverse pressure gradient which separates the upstream boundary layer and produces a separation vortex. The A-type vortex and separation shock always appear together.

(2) B-type vortex: the vortex-induced by an incident shock. The generation mechanism of the B-type vortex is the same as the reflected shock. As shown in Figure 22c, the separation shock of the shroud impacts the vehicle and causes boundary layer separation

which results in the separation vortex. The B-type vortex and reflected shock always appear together. As the shock wave could be reflected many times between the shroud and the vehicle, there are also many small B-type vortexes near the wall.

(3) C-type vortex: the vortex caused by a cavity. The upper shroud and the lower shroud are not completely symmetrical, the upper shroud contains a nose cone which likens a cavity. As shown in Figure 22d, when the high-speed flow passes through the cavity, a separation vortex is generated.

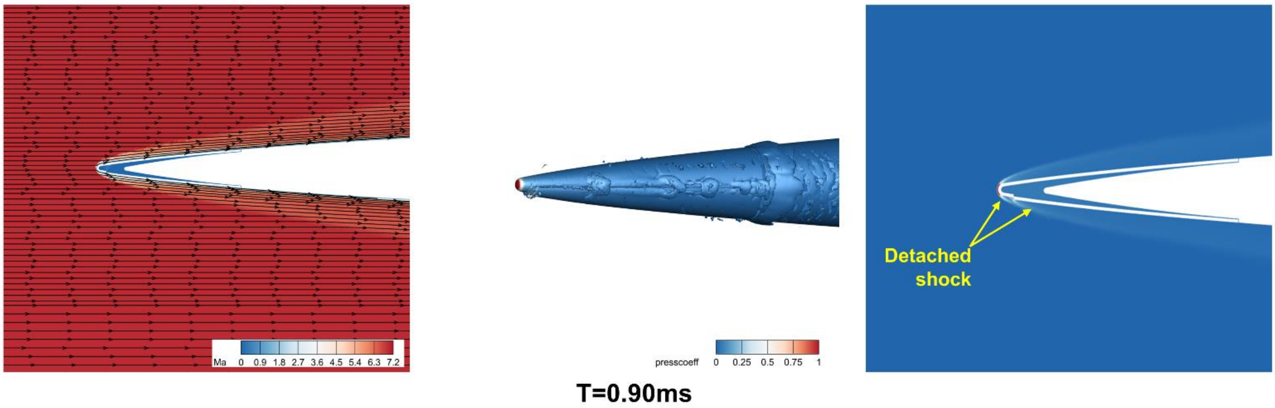

Figure 18. The contour of the streamline and Mach number (**left**), iso-surface of Q-criterion (**middle**), and the contour of the pressure coefficient (**right**) at T = 0.90 ms.

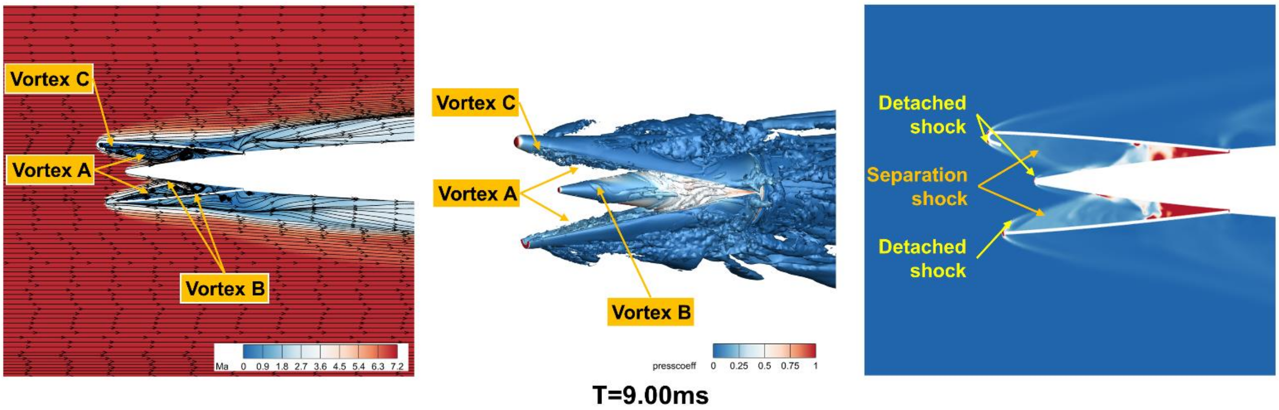

Figure 19. The contour of the streamline and Mach number (**left**), iso-surface of Q-criterion (**middle**), and the contour of the pressure coefficient (**right**) at T = 9.00 ms.

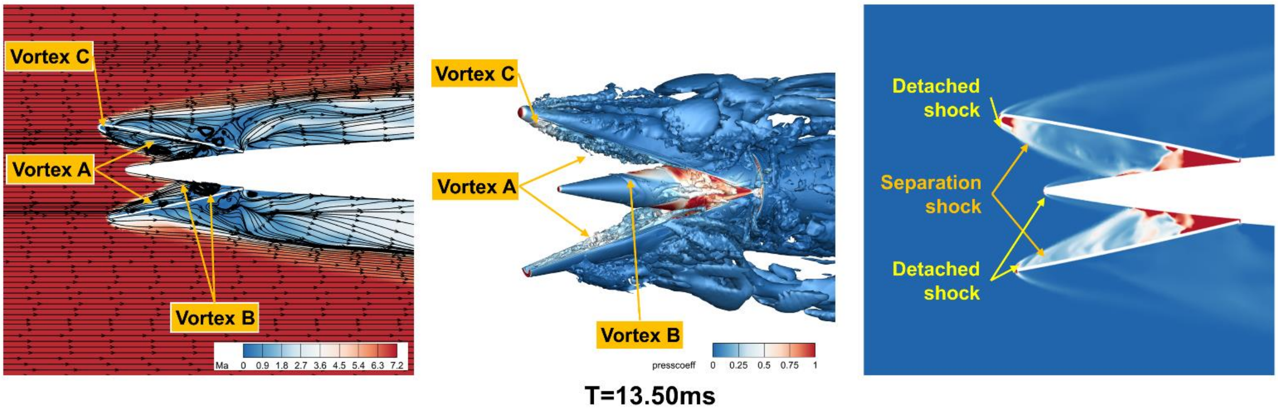

Figure 20. The contour of the streamline and Mach number (**left**), iso-surface of Q-criterion (**middle**), and the contour of the pressure coefficient (**right**) at T = 13.50 ms.

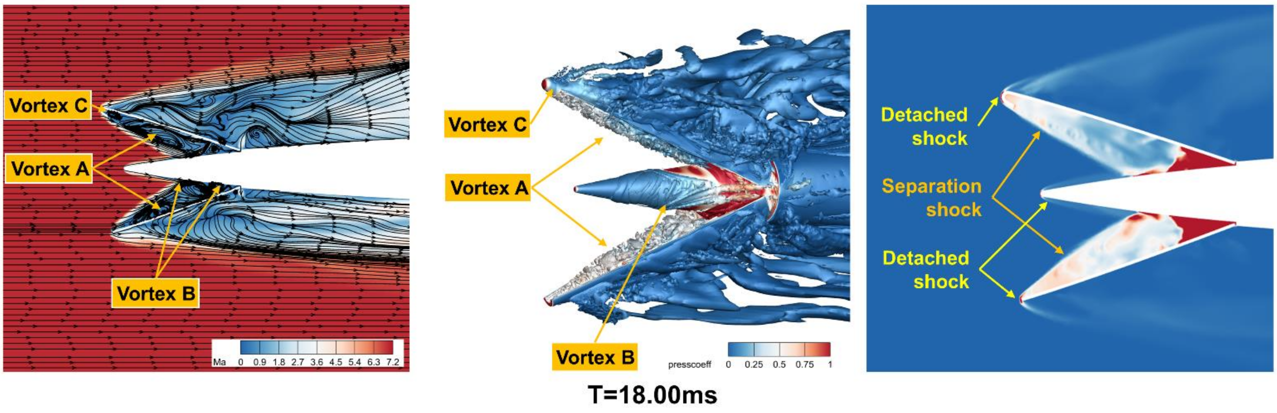

Figure 21. The contour of the streamline and Mach number (**left**), iso-surface of Q-criterion (**middle**), and the contour of the pressure coefficient (**right**) at T = 18.00 ms.

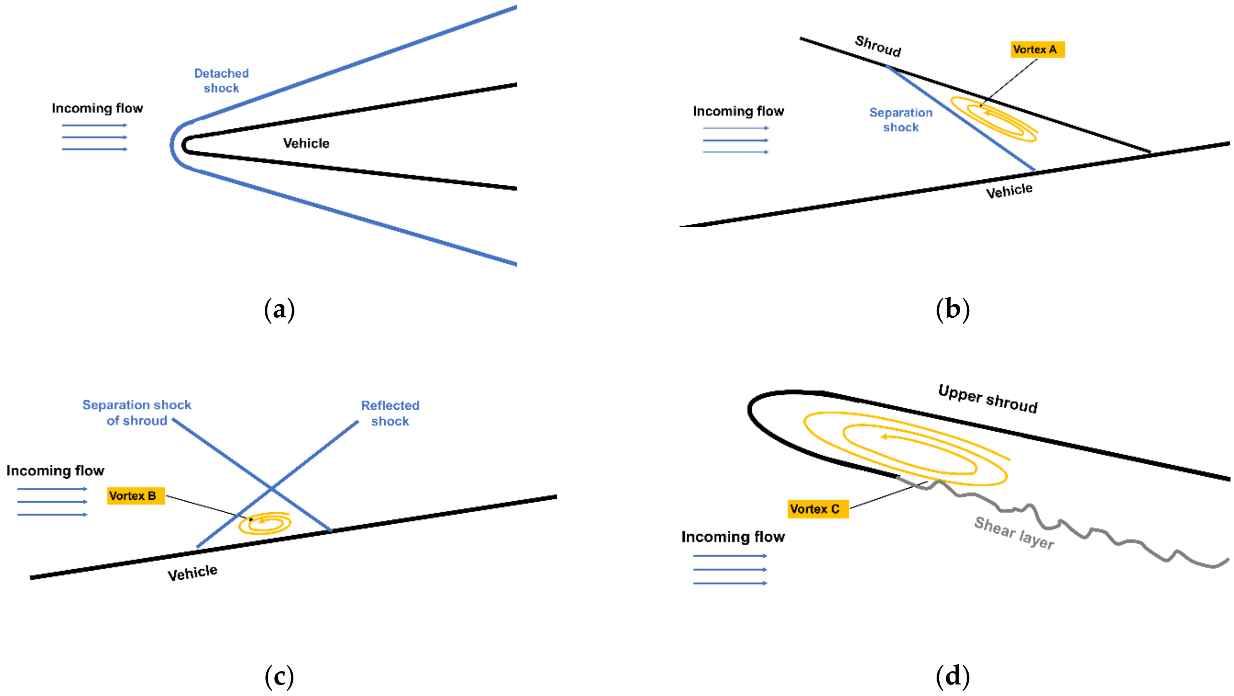

Figure 22. Schematic diagrams of the generation mechanism of shocks and vortexes in the area inside the shrouds: (**a**) detached shock; (**b**) separation shock and A-type vortex; (**c**) reflected shock and B-type vortex; and (**d**) C-type vortex.

It can be seen from Figures 18–21 that, among the three types of vortexes, the A-type vortex has the largest proportion and its boundary is the separation shock. The B-type vortex exists near the wall, and the C-type vortex is near the nose cone of the upper shroud. As shown in Figures 19–21, there is also a strong separation flow and many large-scale vortexes on the leeward side of the shroud. Again, this is essentially a flow separation issue in a large attack angle, and there already is significant detailed and deep research about this. Therefore, this paper only focuses on the unsteady shock wave/vortex/boundary layer interaction in the area inside the shrouds.

At T = 9.00 ms, an A-type vortex is located inside the shroud. As time goes on, the blocking effect of the shroud becomes more and more obvious, and the stronger adverse pressure gradient generates a larger separation vortex; in other words, an A-type vortex expands inside the shroud. At T = 13.50 ms, the A-type vortex is still expanding, which pushes the separation shock further upstream. Additionally, the C-type vortex inside the upper shroud is squeezed into a small space inside the nose cone. At T = 18.00 ms, the

A-type vortex further expands due to the blocking effect of the shroud. It can be seen that almost all the inside surfaces of shrouds are covered by the A-type vortex, and the separation shock is pushed to the head of the shroud. However, the A-type vortex is still in the area between the shroud and its separation shock, and there is only a detached shock in the head of the vehicle.

In summary, there are three main types of vortexes in the area inside the shrouds and the A-type vortex has the largest proportion. The A-type vortex expands inside the shrouds due to the blocking effect of shrouds and strong adverse pressure gradient, which also pushes the separation shock upstream.

4.2.2. Transfer of A-Type Vortex

It can be seen from Figure 17 that within a very small time window, from 18.53 ms to 24.05 ms, there is a strong disturbance in the aerodynamic characteristics of the shrouds. At T = 18.53 ms, both the upper and lower shroud are still locked with the vehicle, therefore, the strong disturbance of the aerodynamic characteristics is not caused by the unlocking of the shrouds. The flow characteristics at typical moments during 18.53 ms to 24.05 ms are presented in Figures 23–26; it can be seen that there is an obvious transfer of the A-type vortex. The A-type vortex transfers from the inside of the shrouds to the boundary layer of the vehicle, which is the result of strong interactions between the A-type vortex, shock wave, and boundary layer.

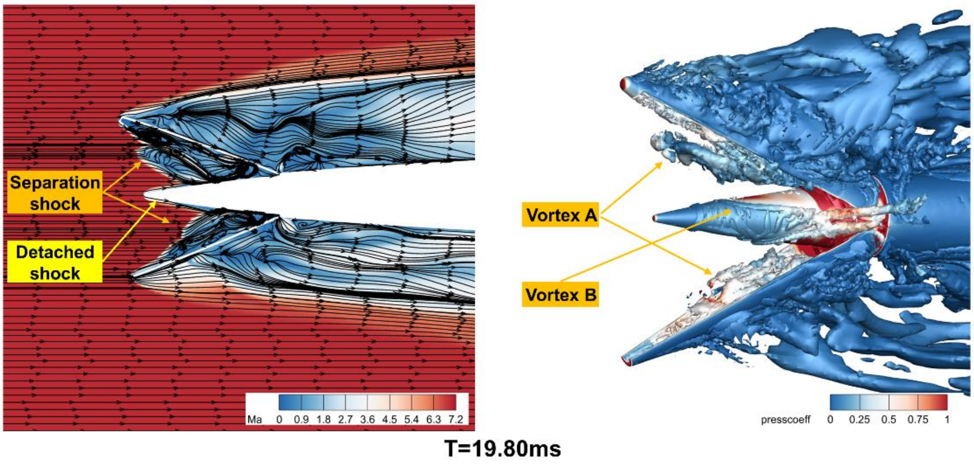

Figure 23. The contour of streamline and Mach number (**left**), and iso-surface of Q-criterion (**right**) at Time = 19.80 ms.

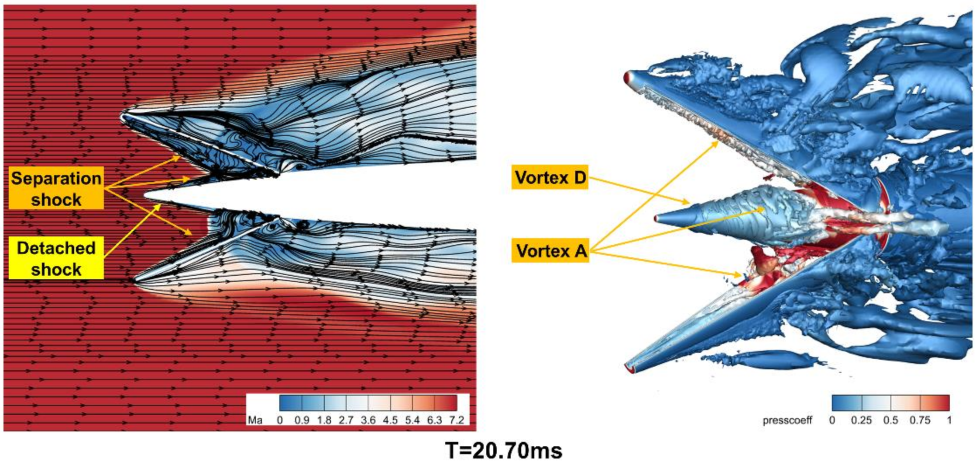

Figure 24. The contour of streamline and Mach number (**left**), and iso-surface of Q-criterion (**right**) at Time = 20.70 ms.

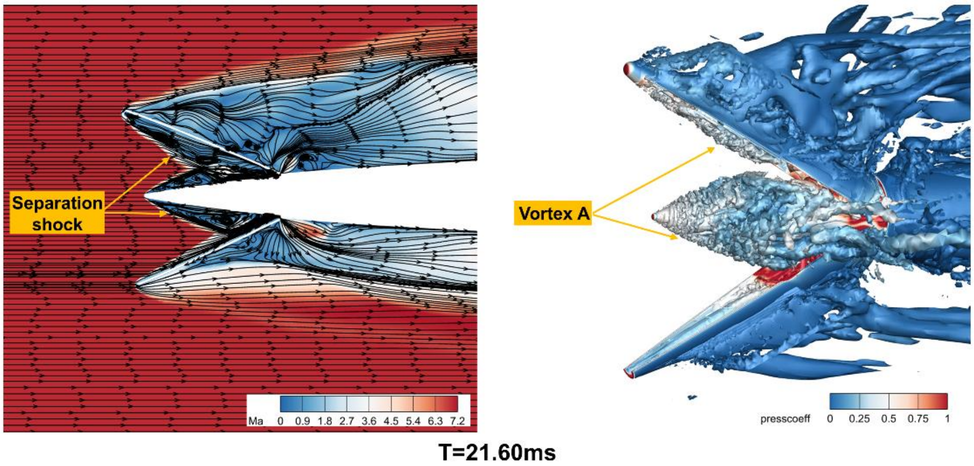

Figure 25. The contour of streamline and Mach number (**left**), and iso-surface of Q-criterion (**right**) at Time = 21.60 ms.

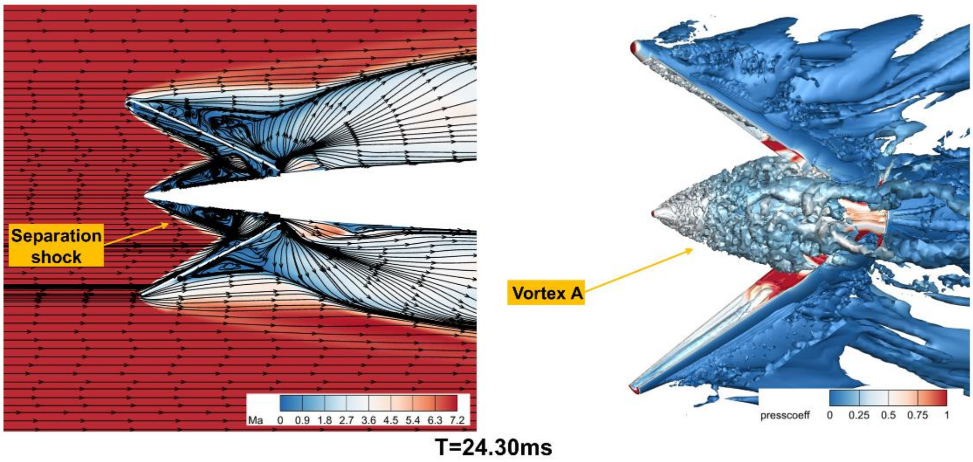

Figure 26. The contour of streamline and Mach number (**left**), and iso-surface of Q-criterion (**right**) at Time = 24.30 ms.

At T = 19.80 ms, the opening angles of the upper and lower shroud are 26.32 degrees and 28.42 degrees, respectively (Figure 23). With the increase in the opening angles of shrouds, the impact of high dynamic pressure flow on the shrouds becomes stronger and stronger, and the blocking effect of shrouds becomes stronger and stronger, as a result, the A-type vortex becomes larger, and larger due to the stronger adverse pressure gradient. It can be seen that the A-type vortex fills the entire shroud, and the boundary of the A-type vortex is the separation shock of the shroud. If the shroud is compared to a "container", this "container" could no longer hold the A-type vortex due to its expansion. As shown in Figure 23, the separation shocks are squeezed to irregular shapes by the A-type vortex at this time.

At T = 20.70 ms, the opening angles of the upper and lower shroud are 27.51 degrees and 29.67 degrees, respectively. As shown in Figure 24, the A-type vortex starts to transfer from the inside of the shrouds into the boundary layer of the vehicle, thus, the boundary layer of the vehicle is obviously thicker than before. Meanwhile, the A-type vortex in the boundary layer of the vehicle produces a separation shock, which is the boundary of the A-type vortex.

It is worth noting that there is also a separation vortex, a D-type of vortex, which is caused by the compression ramp in a hypersonic flow. As shown in Figure 27, the A-type vortex transfers into the boundary layer of the vehicle, which produces a strong separation shock out of the A-type vortex. For the free-stream flow, the combination of an A-type vortex and strong separation shock is similar to a compression ramp on the surface of the vehicle, causing an adverse pressure gradient in the flow field. As a result, the upstream boundary layer of the vehicle is separated and the D-type vortex is generated. However, the scale of the D-type vortex is very small compared with the A-type vortex (Figure 24). An induced weak separation shock is also generated due to the "compression ramp", which dissipates quickly on impact with the high dynamic pressure flow.

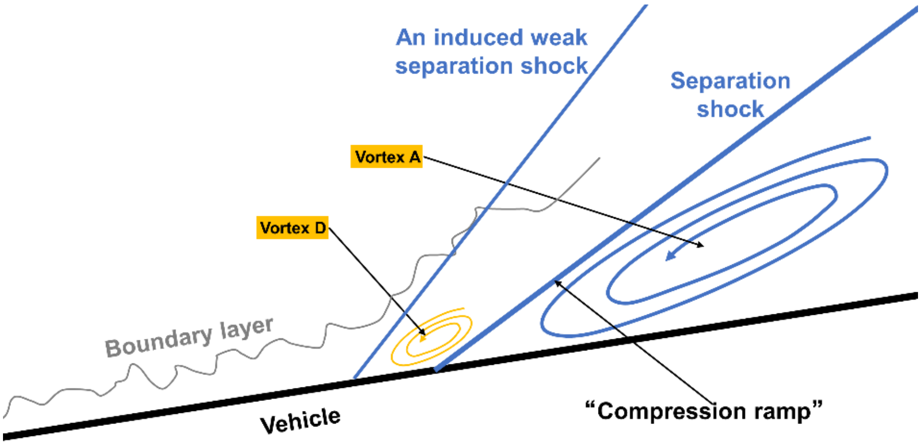

Figure 27. Schematic diagram of the generation mechanism of the D-type vortex.

At T = 21.60 ms, the opening angles of the upper and lower shroud are 28.58 degrees and 30.80 degrees, respectively; the lower shroud unlocks with the vehicle and starts to separate freely, while the upper shroud is still locked with the vehicle. It can be seen from Figure 25 that the A-type vortex transfers from the inside of the shrouds into the boundary layer of the vehicle, and the boundary layer of the vehicle expands rapidly, squeezing the separation shock of the vehicle progressively upstream. As shown in Figure 25, the A-type vortex in the boundary layer of the vehicle forms a large cone in the front of the vehicle, called a "vortex cone" in this paper, which is the result of the strong interactions of the shock wave/vortex/boundary layer during the shroud separation. It can be seen that almost all the surfaces of the vehicle are covered by the A-type vortex and the separation shock is squeezed into the head of the vehicle. The separation speed of the lower shroud is faster than that of the upper shroud; the majority of the A-type vortex inside the lower shroud has transferred into the boundary layer of the vehicle, while the A-type vortex inside the upper shroud has still not completely transferred into the boundary layer of the vehicle at this time.

At T = 24.30 ms, the opening angles of the upper and lower shroud are 31.15 degrees and 33.47 degrees, respectively; both the upper and lower shroud have unlocked with the vehicle and start to separate freely (Figure 26). The majority of the A-type vortex inside the shrouds has transferred into the boundary layer of the vehicle, the boundary layer of the vehicle is still expanding, and the vortex cone is becoming larger and larger.

In summary, the A-type vortex transfers from the inside of the shrouds into the boundary layer of the vehicle from 18.53 ms to 24.05 ms, which makes the boundary layer of the vehicle expand rapidly and produce a large vortex cone; this is the result of the strong interactions of the shock wave/vortex/boundary layer during the shroud separation. The transfer process of the A-type vortex is very fast and finishes within 5.52 ms, however, as shown in Figure 17, the transfer process of the A-type vortex causes a great disturbance to the aerodynamic characteristics.

4.2.3. Dissipation of the Vortex Cone

The shrouds unlock with the vehicle when the opening angle reaches the unlocking angle. The lower shroud first reaches the unlocking angle and unlocks with the vehicle at T = 20.94 ms. The upper shroud reaches the unlocking angle and unlocks with the vehicle a little later at T = 22.96 ms. After unlocking with the vehicle, the shrouds separate freely, driven by the aerodynamic forces. The distance between the shrouds and the vehicle becomes larger and larger during free separation, and the hypersonic flow flows away in the gap between the shrouds and the vehicle. As a result, the A-type vortex inside the vortex cone becomes pushed downstream in the gap by the high dynamic pressure flow. The dissipation process of the vortex cone is presented in Figures 28–31.

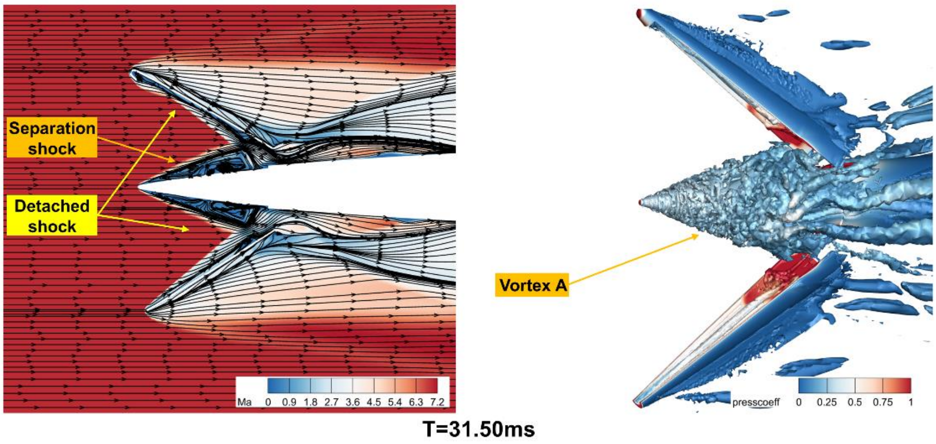

Figure 28. The contour of the streamline and Mach number (**left**), and iso-surface of Q-criterion (**right**) at Time = 31.50 ms.

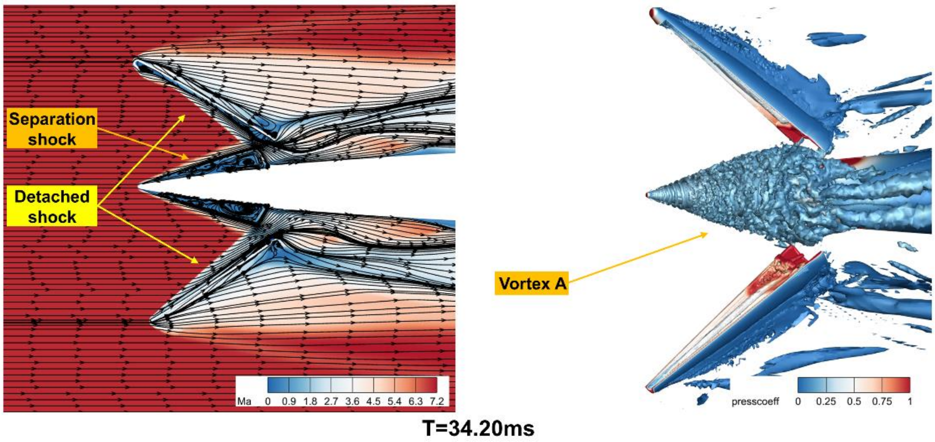

Figure 29. The contour of the streamline and Mach number (**left**), and iso-surface of Q-criterion (**right**) at Time = 34.20 ms.

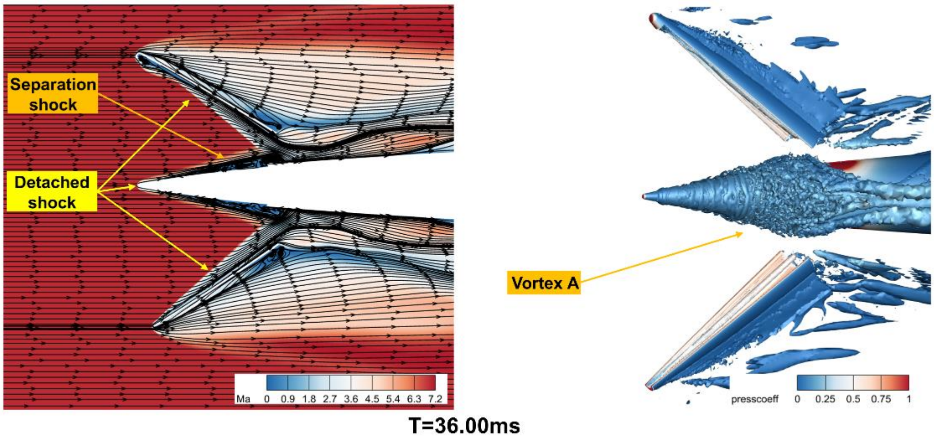

Figure 30. The contour of the streamline and Mach number (**left**), and iso-surface of Q-criterion (**right**) at Time = 36.00 ms.

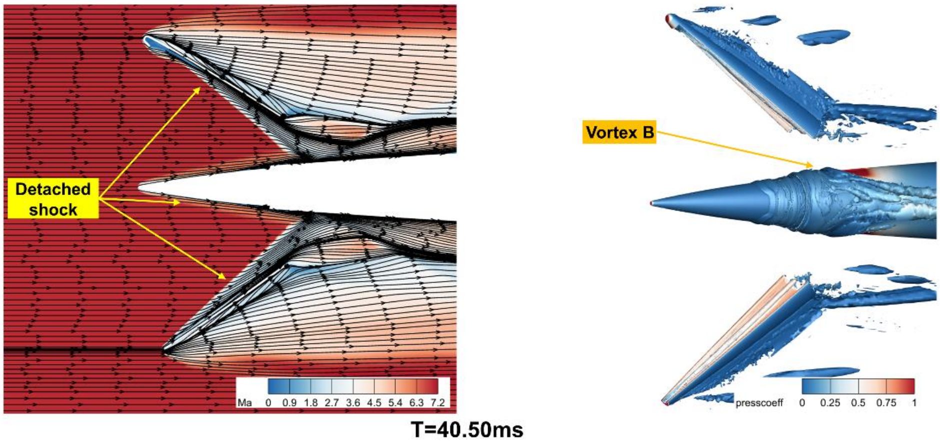

Figure 31. The contour of the streamline and Mach number (**left**), and iso-surface of Q-criterion (**right**) at Time = 40.50 ms.

At T = 31.50 ms, the opening angles of the upper and lower shroud are 34.92 degrees and 38.29 degrees, respectively, and there is an obvious gap between the shroud and the vehicle (Figure 28). Although the vortex cone in the head of the vehicle is still large, the A-type vortex inside the vortex cone is pushed downstream. At T = 34.20 ms, the vortex cone becomes a bit smaller, however, the boundary layer of the vehicle is still full of the A-type vortex (Figure 29).

At T = 36.00 ms, the vortex cone becomes smaller and smaller, the separation shock of the vehicle moves downstream, and a detached shock appears at the head of the vehicle (Figure 30). As shown in Figure 17, the aerodynamic force of the shrouds becomes smooth at 35.36 ms, which could be analyzed by combining the flow fields in Figures 28–31. The A-type vortex in the boundary layer of the vehicle produces a vortex cone, of which, the boundary is a strong separation shock. The strong separation shock impacts the shrouds and causes the disturbance of aerodynamic force. With the dissipation of the vortex cone, the separation shock of the vehicle moves downstream and it no longer impacts the shrouds from 35.36 ms, making the aerodynamic force of the shrouds smooth. At T = 40.50 ms, there are no longer large-scale vortexes in the area inside the shrouds, the A-type vortex has been pushed downstream, and the vortex cone vanishes Figure 31.

4.3. Discussions

4.3.1. The Flow Characteristics during Shroud Separation

Shock wave/turbulent boundary layer interaction occurs in a wide range of supersonic and hypersonic flows, and, as shown in Figure 32, there are three canonical configurations: compression ramp, incident shock, and blunt fin [45,46], and the majority of shock wave/turbulent boundary layer interactions could be obtained on the basis of these three types of configurations.

The shroud separation process in this study includes all three typical shock wave/boundary layer interactions. First, as shown in Figure 22b, at the beginning of shroud separation, the vehicle is like a “blunt fin”, blocking the flow and creating a strong adverse pressure gradient. As a result, the A-type vortex and separation shock are generated. Second, as shown in Figure 22c, the separation shock of the shroud impacts the surface of the vehicle, which is an incident shock for the vehicle. The incident shock causes boundary layer separation, which produces a B-type vortex and reflected shock. In addition, in the transfer process of the A-type vortex from the inside of shrouds into the boundary layer of the vehicle, as shown in Figure 27, for the free-stream flow, the combination of the A-type vortex and strong separation shock is similar to a compression ramp in the surface of the vehicle, which causes an adverse pressure gradient in the flow field. As a result, the upstream boundary layer of the vehicle is separated and the D-type vortex is generated.

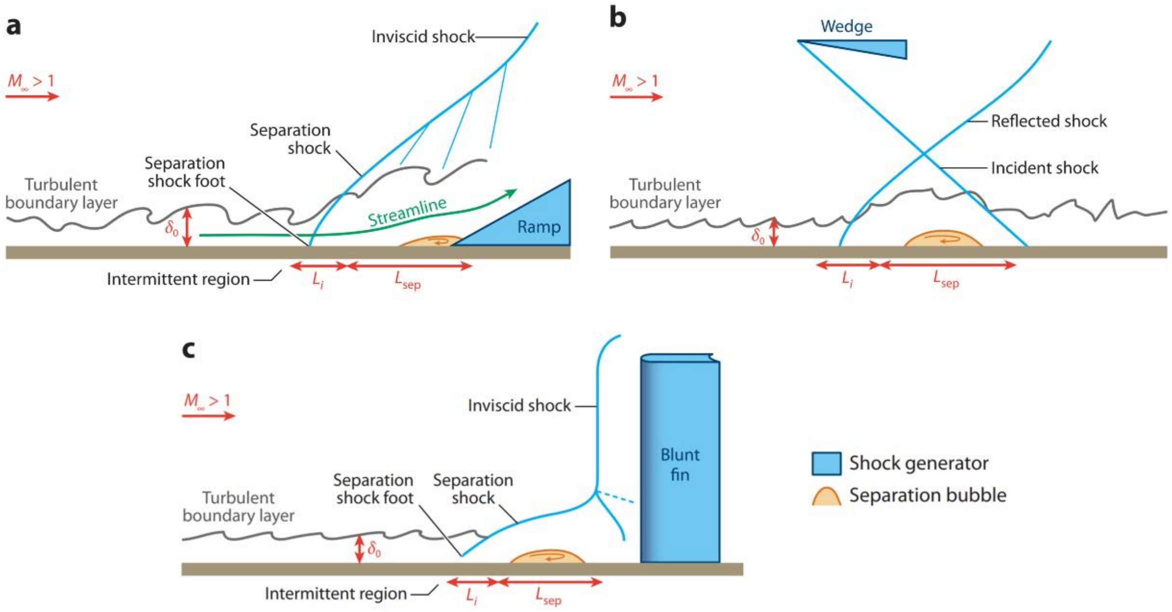

Figure 32. Schematic diagrams of the three typical shock wave/boundary layer interactions [45]: (**a**) compression ramp; (**b**) reflected shock; (**c**) blunt fin. Figure adapted with permission from Clemens et al. (2014). Copyright © 2014 Annual Reviews.

There are four types of separation vortexes and three types of shock waves in the area inside the shrouds during the hypersonic shroud separation, causing complex shock wave/vortex/turbulent boundary layer interactions. The four types of separation vortexes include the A-type vortex caused by the blocking effect of shrouds and vehicles, the B-type vortex induced by the incident shock, the C-type vortex caused by the cavity, and the D-type vortex induced by the compression ramp. The A-type vortex has the largest proportion, the B-type vortex and D-type vortex are located near the wall, and the C-type vortex is near the nose cone of the upper shroud. The three types of shock waves include detached shock, separation shock, and reflected shock. As shown in Figures 19–21, there are also strong separation flows and many large-scale vortexes on the leeward side of the shroud, which is essentially a flow separation issue at a large attack angle. There is already significant detailed and deep research about this, therefore, this paper only focuses on the unsteady shock wave/vortex/boundary layer interactions in the area inside the shrouds.

Wang also studied the shroud separation with a hypersonic air-breathing vehicle based on unsteady Reynolds-averaged Navier–Stokes equations (RANS) [5], although the research model is different from the axisymmetric hypersonic vehicle model in this study, it still can be seen that the results of IDDES and RANS are quite different. The IDDES method can provide more unsteady flow characteristics in detail and could be used to analyze the strong and complicated shock/vortex/boundary layer interactions; it is a huge advantage over the RANS method.

4.3.2. The Expansion-Transfer-Dissipation of the A-Type Vortex

An unsteady process of expansion-transfer-dissipation of the A-type vortex is found during the hypersonic shroud separation, the result of strong interactions between the A-type vortex, shock wave, and boundary layer.

The generation and expansion mechanisms of the A-type vortex are presented in Figures 18–22, the high dynamic pressure flow is blocked by the shroud and creates a strong adverse pressure gradient, which separates the upstream boundary layer and produces the A-type vortex. As time goes on, the blocking effect of the shrouds becomes more and more obvious, and the stronger adverse pressure gradient generates a larger separation vortex; the A-type vortex expands inside the shroud, which pushes the separation shock further upstream.

Then, as shown in Figures 23–26, the shroud can no longer hold the A-type vortex due to its expansion, and the separation shocks are squeezed into irregular shapes by the A-type vortex. Then, the A-type vortex transfers from the inside of the shrouds into the boundary layer of the vehicle, producing a large cone in the front of the vehicle we call a "vortex cone". The vortex cone squeezes the separation shock of the vehicle upstream.

Then, the shrouds unlock with the vehicle and separate freely, driven by the aerodynamic forces, and the hypersonic flow flows away in the gap between the shrouds and the vehicle. As a result, as shown in Figures 28–31, the A-type vortex inside the vortex cone is pushed downstream in the gap by the high dynamic pressure flow. Finally, all the A-type vortex is pushed downstream and the vortex cone vanishes.

4.3.3. The Generation and Transfer Mechanisms of the A-Type Vortex

There are still two interesting issues:

(1) Why is the A-type vortex generated in the inside of the shroud rather than directly generated in the boundary layer of the vehicle at the beginning of separation?

(2) Why does the A-type vortex transfer from the inside of shrouds into the boundary layer of the vehicle?

The adverse pressure gradient is the reason for the generation and transfer of the A-type vortex. As shown in Figures 18–22, at the beginning of shroud separation, the pressure on the surface of the vehicle is obviously larger than that on the shrouds, therefore the separation vortex is generated more easily in the inside of the shroud rather than in the boundary layer of the vehicle. With the increase in the opening angles of the shrouds, the impact of the high dynamic pressure flow on the shrouds becomes stronger and stronger, and the blocking effect of shrouds becomes stronger and stronger. As a result, as shown in Figures 28–31, the pressure on the shrouds increases rapidly and becomes larger than that on the vehicle. When the pressure on the shrouds is strong enough, the A-type vortex inside of the shrouds is squeezed into the boundary layer of the vehicle. Therefore, the adverse pressure gradient is the root cause driving the generation and transfer of the A-type vortex during the shroud separation.

5. Conclusions

In order to reveal the flow structure and mechanism of hypersonic shroud separation, the unsteady multi-body separation characteristics and flow characteristics of shroud separation at Mach 7.0 are investigated based on numerical simulation. The IDDES method, dynamic hybrid overset mesh method, and HLLE++ scheme are utilized to ensure numerical accuracy. The following conclusions can be drawn:

(1) The numerical methods in this paper have been fully validated, including mesh independency verification, time independency verification, IDDES method verification, and wind tunnel experiment validation of hypersonic multi-bodies separation, indicating that the numerical methods in this paper are suitable for the hypersonic shroud separation.

(2) The shrouds have been moving away from the vehicle during the separation process and separate from the vehicle safely within 75 ms. There are four types of separation vortexes and three types of shock waves in the area inside the shrouds during the hypersonic shroud separation which generate complex shock wave/vortex/boundary layer interactions. The shroud separation process includes all three canonical shock wave/boundary layer interactions: compression ramp, incident shock, and blunt fin.

(3) The A-type vortex has the largest proportion among the four types of separation vortexes. An unsteady process of expansion-transfer-dissipation of the A-type vortex during the hypersonic shroud separation was found, the result of strong interactions between the A-type vortex, separation shock, and boundary layer. The adverse pressure gradient is the root cause driving the generation and transfer of the A-type vortex during the shroud separation.

(4) The transfer process of the A-type vortex only lasts for 5.52 ms, but it causes a large disturbance to the aerodynamic force which should be taken into consideration in the design of the hypersonic vehicle.

A hypersonic vehicle in low-altitudes near space is a new research field in recent years, and the unsteady shock wave/vortex/turbulent boundary layer interactions of hypersonic shroud separation are investigated in this paper. The results of this paper could provide a reference for the design of near-space hypersonic vehicles. The time of hypersonic shroud separation is very short (within 75 ms), therefore, the shroud is treated as a rigid body in this study. The aerothermal and aeroelastic influence will be taken into consideration in consequent research.

Author Contributions: Conceptualization, P.C. and G.Z.; data curation, P.C. and H.L.; formal analysis, P.C., H.L. and J.T.; funding acquisition, P.C. and X.W.; investigation, P.C. and G.Z.; methodology, P.C., J.C. and J.T.; project administration, P.C. and X.W.; resources, P.C.; software, P.C. and H.J.; supervision, M.M.; validation, X.W. and M.M.; visualization, P.C. and X.W.; writing—original draft, P.C.; writing—review and editing, P.C. and J.C. All authors have read and agreed to the published version of the manuscript.

Funding: This research was funded by the National Numerical Wind Tunnel (No. PZT20190006), the National Natural Science Foundation of China (No. 12102453), and the internal fund of the China Aerodynamics Research and Development Center (No. PZT20200099).

Informed Consent Statement: Not applicable.

Conflicts of Interest: The authors declare no conflict of interest.

Nomenclature

P_{∞}	Pressure of free-stream flow
T_{∞}	Temperature of free-stream flow
Mach	Mach number
DES	Detached-eddy simulation
DDES	Delayed detached-eddy simulation
IDDES	Improved delayed-detached-eddy simulation
δ	The thickness of the boundary layer
C_{l}	Lift coefficient
C_{d}	Drag coefficient
M_{y}	Pitching moment coefficient
L/D	Lift–drag ratio
Ω	Volume of the control volume
$\boldsymbol{Q}$	Conservative state vector
$\vec{\boldsymbol{v}}_g$	Wall velocity
$\vec{\boldsymbol{n}}$	Outward-pointing normal unit vector
$\boldsymbol{H}(\boldsymbol{Q})$	Inviscid flux vector
$\boldsymbol{H}_v(\boldsymbol{Q})$	Viscous flux vector
ρ	Density
E	Total energy
V	Contravariant velocity
p	Pressure
τ	Viscous stress
l_{RANS}	RANS length scale
l_{WMLES}	WMLES length scale
λ^{HLLE++}	Eigenvalue of HLLE++
λ^{HLLE+}	Eigenvalue of HLLE+
β	Switching function
k_p	Pressure gradient-based switch sensor

References

1. Xu, S.; Wang, Y.; Wang, Z.; Fan, X.; Zhao, X. Design and analysis of a hypersonic inlet with an integrated bump/forebody. *Chin. J. Aeronaut.* **2019**, *32*, 2267–2274. [CrossRef]
2. JIANG, Z.; Zhang, Z.; Liu, Y.; Wang, C.; Luo, C. The criteria for hypersonic airbreathing propulsion and its experimental verification. *Chin. J. Aeronaut.* **2020**, *34*, 94–104. [CrossRef]
3. Kimmel, R.L.; Adamczak, D.W.; Hartley, D.; Alesi, H.; Frost, M.A.; Pietsch, R.; Shannon, J.; Silvester, T. Hypersonic International Flight Research Experimentation-5b Flight Overview. *J. Spacecr. Rocket.* **2018**, *55*, 1303–1314. [CrossRef]
4. Available online: https://baike.baidu.com/item/HTV-2/9231692?fr=aladdin (accessed on 1 September 2022).
5. Wang, S.; Li, C.; Chen, W. Numerical investigation on unsteady flows with an air-breathing hypersonic vehicle during its shroud separation. In Proceedings of the 21st AIAA International Space Planes and Hypersonics Technologies Conference, Xiamen, China, 6–9 March 2017. AIAA-2017-2335.
6. Guthrie, M.; Ross, M.R. Deriving transmissibility functions with finite elements for specifications. *J. Spacecr. Rocket.* **2022**, *59*, 271–285. [CrossRef]
7. Zaitsev, B.P.; Protasova, T.V.; Smetankina, N.V.; Klymenko, D.V.; Larionov, I.F.; Akimov, D.V. Oscillations of the payload fairing body of the cyclone-4 m launch vehicle during separation. *Strength. Mater.* **2021**, *52*, 849–863. [CrossRef]
8. Whalley, I. Development of the STARS II shroud separation system. In Proceedings of the 37th Joint Propulsion Conference and Exhibit, Salt Lake City, UT, USA, 8–11 July 2001. AIAA-2001-3769.
9. Tsutsumi, S.; Takaki, R.; Takama, Y.; Imagawa, K.; Nakakita, K.; Kato, H. Hybrid LES/RANS simulations of transonic flow-field around a rocket fairing. In Proceedings of the 30th AIAA Applied Aerodynamics Conference, New Orleans, LA, USA, 25–28 June 2012. AIAA-2012-2900.
10. Dagan, Y.; Arad, E. Analysis of shroud release applied for high-velocity missiles. *J. Spacecr. Rocket.* **2014**, *51*, 57–65. [CrossRef]
11. Chamberlain, R. Time-accurate calculation of the HEDI shroud separation event. In Proceedings of the Annual Interceptor Technology Conference, Huntsville, AL, USA, 19–21 May 1992. AIAA-92-2775.
12. Raj, A.; Anandhanarayanan, K.; Krishnamurthy, R.; Chakraborty, D. Numerical simulation of fairing separation test for hypersonic air breathing vehicle. *Proc. Inst. Mech. Eng. Part G J. Aerosp. Eng.* **2016**, *231*, 319–325. [CrossRef]
13. Zhong, Q.; Fan, Y.; Wu, W. A switching-based control method for the fairing separation control of axisymmetric hypersonic vehicles. *Aerospace* **2022**, *9*, 132. [CrossRef]
14. Holden, M.; Smolinski, G.; Mundy, E.; MacLean, M.; Wadhams, T.; Walker, B. Experimental studies for hypersonic vehicle design and code validation of unsteady flow characteristics associated with "free flight" shroud and stage separation, and mode switching. In Proceedings of the 46th AIAA Aerospace Sciences Meeting and Exhibit, Reno, NV, USA, 7–10 January 2008. AIAA-2008-642.
15. Hong, Y.; Li, Z.; Yang, J. Scaling of interaction lengths for hypersonic shock wave/turbulent boundary layer interactions. *Chin. J. Aeronaut.* **2021**, *34*, 504–509. [CrossRef]
16. Ben, H.S.I.; Fournier, G.; Tenaud, C. On the Behaviour of High-Order One-Step Monotonicity-Preserving Scheme for Direct Numerical Simulation of Shocked Turbulent Flows. *Int. J. Comput. Fluid Dyn.* **2020**, *34*, 671–704.
17. Available online: https://baijiahao.baidu.com/s?id=1646388275128676313 (accessed on 5 September 2022).
18. Chen, J.; Wu, X.; Zhang, J.; Li, B.; Jia, H.; Zhou, N. FlowStar: A general unstructured-grid CFD software of National Numerical Windtunnel (NNW) project. *Acta Aeronaut. Astronaut. Sin.* **2021**, *42*, 625739.
19. Tang, J.; Cui, P.; Li, B.; Zhang, Y.; Si, H. Parallel hybrid mesh adaptation by refinement and coarsening. *Graph. Models* **2020**, *111*, 101084. [CrossRef]
20. Tang, J.; Ma, M.; Li, B.; Cui, P. A local and fast interpolation method for mesh deformation. *Prog. Comput. Fluid Dyn.* **2019**, *19*, 282–292. [CrossRef]
21. Cui, P.; Zhou, G.; Zhang, Y.; Jia, H.; Wu, X.; Ma, M.; Li, H.; Chen, B. Improved Delayed Detached-Eddy Investigations on the Flow Control of the Leading-Edge Flat Spoiler of the Cavity in the Low-Aspect-Ratio Aircraft. *Aerospace* **2022**, *9*, 526. [CrossRef]
22. Tang, J.; Zhang, J.; Li, B.; Zhou, N. Unsteady flow simulation with mesh adaptation. *Int. J. Mod. Phys. B* **2020**, *34*, 2040080. [CrossRef]
23. Tang, J.; Zhang, J.; Li, B.; Cui, P.; Zhou, N. Parallel algorithms for unstructured hybrid mesh adaptation. *Acta Aeronaut. Astronaut. Sin.* **2020**, *41*, 123202.
24. Cui, P.; Li, B.; Tang, J.; Chen, J.; Deng, Y. A modified adjoint-based grid adaptation and error correction method for unstructured grid. *Int. J. Mod. Phys. B.* **2018**, *32*, 1840020. [CrossRef]
25. Cui, P.; Deng, Y.; Tang, J.; Li, B. Adjoint equations-based grid adaptation and error correction. *Acta Aeronaut. Astronaut. Sin.* **2016**, *37*, 2992–3002.
26. Venkatakrishnan, V. On the accuracy of limiters and convergence to steady state solutions. In Proceedings of the 31st Aerospace Sciences Meeting, Reno, NV, USA, 11–14 January 1993. AIAA-93-0880.
27. Xue, Y.; Wang, L.; Fu, S. Detached-eddy simulation of supersonic flow past a spike-tipped blunt nose. *Chin. J. Aeronaut.* **2018**, *31*, 1815–1821. [CrossRef]
28. Boudreau, M.; Dumas, G.; Veilleux, J.C. Assessing the ability of the DDES turbulence modeling approach to simulate the wake of a bluff body. *Aerospace* **2017**, *4*, 41. [CrossRef]
29. Krishnan, V.; Squires, K.D.; Forsythe, J.R. Prediction of separated flow characteristics over a hump. *AIAA J.* **2006**, *42*, 252–262. [CrossRef]

30. Wang, H.; Li, J.; Jin, D.; Dai, H.; Gan, T.; Wu, Y. Effect of a transverse plasma jet on a shock wave induced by a ramp. *Chin. J. Aeronaut.* **2017**, *30*, 1854–1865. [CrossRef]
31. Tramel, R.; Nichols, R.; Buning, P. Addition of improved shock-capturing schemes to OVERFLOW 2.1. In Proceedings of the 19th AIAA Computational Fluid Dynamics, San Antonio, TX, USA, 22–25 June 2009. AIAA-2009-3988.
32. Zhang, P.; Luo, L.; Jia, H.; Zhao, W.; Zhang, Y.; Wu, X. Application of HLLE++ scheme in the simulation of high Mach number cavity flow. *Chin. J. Comput. Mech.* **2021**. Available online: https://kns.cnki.net/kcms/detail/21.1373.O3.20210925.1031.018.html (accessed on 26 September 2021).
33. Zhang, P.; Cheng, X.; Chen, H.; Jia, H.; Luo, L.; Tang, Y. Study on unsteady flow mechanism of high Mach number cavity. *J. B. Univ. Aeronaut. Astronaut* **2022**. Available online: https://doi.org/10.13700/j.bh.1001-5965.2021.0609 (accessed on 10 March 2022).
34. McDaniel, D.R.; Nichols, R.H.; Eymann, T.A.; Starr, R.E.; Morton, S.A. Accuracy and Performance Improvements to Kestrel's Near-Body Flow Solver. In Proceedings of the 54th AIAA Aerospace Sciences Meeting, San Diego, CA, USA, 4–8 January 2016. AIAA-2016-1051.
35. Bond, R.B.; Nichols, R.; Power, G.D. Extension of Kestrel to General Thermochemical Models, Part, I. In Proceedings of the 46th AIAA Thermophysics Conference, Washington, DC, USA, 13–17 June 2016. AIAA-2016-4435.
36. Blazek, J. *Computational Fluid Dynamics: Principles and Applications*, 1st ed.; Elsevier: Oxford, UK, 2001; pp. 181–216.
37. Cui, P.; Li, B.; Tang, J.; Gong, X.; Ma, M. An improved tri-linear interpolation method for hybrid overset grids and its application. In Proceedings of the Asia-Pacific International Symposium on Aerospace Technology, Chengdu, China, 16–18 October 2018.
38. Cui, P.; Tang, J.; Li, B.; Ma, M.; Deng, Y. Conservative interpolation method of overlapping grids based on super grids. *Acta Aeronaut. Astronaut. Sin.* **2018**, *39*, 121596.
39. Mancini, S.; Kolb, A.; Gonzalez-Martino, I.; Casalino, D. Very-Large Eddy Simulations of the M219 Cavity at High-Subsonic and Supersonic Conditions. In Proceedings of the AIAA Scitech 2019 Forum, San Diego, CA, USA, 7–11 January 2019. AIAA-2019-1833.
40. Lyubimov, D.; Fedorenko, A. External flow velocity and synthetic jets parameters influence on cavity flow structure and acoustics characteristics using RANS/ILES. *Int. J. Aeroacoust.* **2018**, *17*, 259–274. [CrossRef]
41. Yan, P.; Zhang, Q.; Li, J. Numerical study of strong interplay between cavity and store during launching. *J. Mech.* **2018**, *34*, 103–112. [CrossRef]
42. Mancini, S.; Kolb, A.; Gonzalez-Martino, I.; Casalino, D. Predicting high-speed feedback mechanisms in rectangular cavities using lattice-Boltzmann very-large eddy simulations. *Aerosp. Sci. Technol.* **2021**, *117*, 106908. [CrossRef]
43. Allen, R.; Mendonca, F. DES Validations of Cavity Acoustics over the Subsonic to Supersonic Range. In Proceedings of the 10th AIAA/CEAS Aeroacoustics Conference, Manchester, Great Britain, UK, 10–12 May 2004. AIAA-2004-2862.
44. Lin, J.; Wang, X.; Zhong, J.; Xie, Z.; Pi, Y.; Zhao, J. Investigation and application of high Mach number multi-body separation test technique. *J. Propuls. Technol.* **2020**, *41*, 925–933.
45. Clemens, N.T.; Narayanaswamy, V. Low frequency unsteadiness of shock wave/turbulent boundary layer interactions. *Annu. Rev. Fluid Mech.* **2014**, *46*, 469–492. [CrossRef]
46. Fan, X.; Tang, Z.; Wang, G.; Yang, Y. Review of low-frequency unsteadiness in shock-wave/turbulent boundary-layer interaction. *Acta Aeronaut. Astronaut. Sin.* **2022**, *43*, 625917.